# Downregulation of Dickkopf-3, a Wnt antagonist elevated in Alzheimer's disease, restores synapse integrity and memory in a disease mouse model


## AUTHORS

Nuria Martin-Flores[1,4], Marina Podpolny[1,4], Faye McLeod[1], Isaac Workman[1], Karen Crawford[2], Dobril Ivanov[2], Ganna Leonenko[2], Valentina Escott-Price[2,3], Patricia C. Salinas[1]*

## Affiliations

[1] Department of Cell and Developmental Biology, Division of Biosciences, University College London, UK

[2] Division of Psychological Medicine and Clinical Neurosciences, Cardiff University, UK

[3] UK Dementia Research Institute, Cardiff University, UK

[4] These authors contributed equally to this work

* Corresponding author. Correspondence: Professor Patricia C. Salinas, p.salinas@ucl.ac.uk

## ABSTRACT

Increasing evidence supports a role for deficient Wnt signaling in Alzheimer's disease (AD). Studies reveal that the secreted Wnt antagonist Dickkopf-3 (DKK3) colocalizes to amyloid plaques in AD patients. Here, we investigate the contribution of DKK3 to synapse integrity in healthy and AD brains. Our findings show that DKK3 expression is upregulated in the brains of AD subjects and that DKK3 protein levels increase at early stages in the disease. In hAPP-J20 and hAPP$^{NL-G-F/NL-G-F}$ AD models, extracellular DKK3 levels are increased and DKK3 accumulates at dystrophic neuronal processes around plaques. Functionally, DKK3 triggers the loss of excitatory synapses through blockade of the Wnt/GSK3β signaling with a concomitant increase in inhibitory synapses signaling via activation of the Wnt/JNK pathway. In contrast, DKK3 knockdown restores synapse number and memory in hAPP-J20 mice. Collectively, our findings identify DKK3 as a novel driver of synaptic defects and memory impairment in AD.

## KEYWORDS

Alzheimer's disease, Wnt signaling, Dickkopf, synapse, synapse degeneration, amyloid plaques, memory, hAPP-J20, hAPP$^{NL-G-F/NL-G-F}$

## INTRODUCTION

Alzheimer's disease (AD) is the most common form of dementia in the aging population. The disease is characterized by progressive synaptic dysfunction and loss, early signatures that correlate with cognitive decline in AD and precede both neuronal death and the onset of severe dementia by at least 10 years (Mucke and Selkoe, 2012; Selkoe and Hardy, 2016). Current AD models suggest that amyloid-β (Aβ) initiates a pathophysiological cascade leading to synapse failure and eventually cognitive decline. Although the primary neuropathological hallmarks of AD are amyloid plaques and neurofibrillary tangles, soluble Aβ oligomers (Aβo) are considered one of the key toxic proteins driving synapse dysfunction (Mucke and Selkoe, 2012; Selkoe and Hardy, 2016; Walsh et al., 2002). However, the exact mechanisms by which Aβo impair synapse function and cause their degeneration are not fully understood.

Increasing evidence suggests that Wnt signaling is compromised in AD, contributing to synapse degeneration. Wnts are secreted proteins that play a crucial role in synapse formation, synaptic plasticity, and synapse integrity (McLeod and Salinas, 2018). The canonical Wnt pathway is particularly impaired in AD. For example, levels of the secreted Wnt antagonist Dickkopf-1 (DKK1) are increased in the brain of AD patients and AD models (Caricasole et al., 2004; Purro et al., 2012; Rosi et al., 2010). DKK1 promotes synapse degeneration and its blockade protects against Aβ-induced dendritic spine and synapse loss (Marzo et al., 2016; Purro et al., 2012; Sellers et al., 2018). Supporting the role of deficient Wnt signaling in AD, three genetic variants of *LRP6,* a crucial Wnt co-receptor, are linked to late-onset AD and confer decreased Wnt signaling in cell lines (Alarcón et al., 2013; De Ferrari et al., 2007). Notably, mice carrying the *Lrp6*-Valine variant exhibit increased synapse vulnerability during aging and in AD (Jones et al., 2023). Furthermore, loss-of-function of *Lrp6* exacerbates amyloid pathology in an AD mouse model (Liu et al., 2014). In addition, Frizzled-1 (Fz1) and Fz7, Wnt receptors present at synapses, are downregulated in the hippocampus of AD subjects and AD models (Palomer et al., 2022). However, the molecular mechanisms by which deficient Wnt signaling contributes to synaptic defects in AD are poorly understood. Importantly, it remains unexplored whether amelioration of Wnt deficiency restores synaptic connectivity and memory in AD.

Dickkopf-3 (DKK3), a member of the secreted Wnt antagonist DKK family, could contribute to AD pathogenesis. Like other DKKs, DKK3 has two cysteine-rich domains but it also contains an elongated N-terminus with a Soggy domain (Krupnik et al., 1999; Niehrs, 2006). Although studies suggest that DKK3 antagonizes the Wnt canonical pathway (Caricasole et al., 2003; Mizobuchi et al., 2008; Zhu et al., 2014), the function of DKK3 in the adult brain is unclear. *Dkk3* knock-out mice are viable and do not exhibit morphological alterations in the brain, but

female mice manifest hyperlocomotion (Barrantes et al., 2006). Recent findings indicate that DKK3 is increased in plasma, and cerebrospinal fluid (CSF), and accumulates in Aβ plaques in the human AD brain (Bruggink et al., 2015; Drummond et al., 2017; Xiong et al., 2019). However, the impact of DKK3 on synapses and cognitive function, which are affected by deficient Wnt signalling (Jones et al., 2023; Marzo et al., 2016), in AD remains to be studied. Studies on DKK3 in AD would shed new light on the mechanisms that contribute to synapse vulnerability in AD.

Here, we investigate the role of DKK3 in the integrity and function of excitatory and inhibitory synapses in healthy and AD brains. Our RNAseq analyses reveal that *DKK3* expression is increased in the brains of AD patients. Consistently, we found that DKK3 protein is increased in the human AD brain from early stages of the disease. In two AD mouse models, extracellular DKK3 is increased in the hippocampus before substantial plaque deposition. As the pathology progresses in the mouse AD brain, DKK3 accumulates in dystrophic neurites around amyloid plaques. Functionally, our confocal and electrophysiological studies demonstrate that increased levels of DKK3 trigger the loss of excitatory synapses with a concomitant increase in inhibitory synapses in the adult mouse hippocampus through different Wnt pathways. Crucially, *in vivo* downregulation of DKK3 ameliorates excitatory and inhibitory synaptic defects in the hippocampus and improves memory in an AD mouse model. Together, our findings in humans and functional studies in mice identify DKK3 as a driver of synapse pathology and cognitive impairment in AD.

## RESULTS

### DKK3 is increased in the human AD brain

A previous study found that DKK3 is present in Aβ plaques in the brain of AD patients (Bruggink et al., 2015). To investigate whether DKK3 is increased in AD, we examined the expression of *DKK3* in the AD brain using RNA-seq data from the ROSMAP (De Jager et al., 2018), MSBB (Wang et al., 2018), and MayoRNAseq (Allen et al., 2016) datasets (n = 248 controls, 379 AD cases). Logistic regression analyses revealed that *DKK3* was upregulated in AD cases (regression β-coefficient = 0.31; p-value = $1.52 \times 10^{-3}$). In addition, ordinal regression analyses showed that *DKK3* was differentially expressed in relation to Braak scores, a measure of neurofibrillary tangle pathology (Braak et al., 2006) (regression β-coefficient = 0.27; p-value = $8.84 \times 10^{-4}$), but not to CERAD scores, a measure of neuritic plaque density (Mirra et al., 1991) (regression β-coefficient: 0.07; p-value = 0.43) (**Figure 1A**). These results indicate that the expression of *DKK3* is increased in the brain of human AD patients.

99 We next assessed DKK3 protein levels in the hippocampus of AD patients at different disease
100 stages based on their Braak status. We evaluated healthy individuals and patients with Braak
101 stages I-III and IV-VI (n = 16 per group, **Table S1**). Given that DKK3 is found at Aβ plaques in
102 the human AD brain (Bruggink et al., 2015; Drummond et al., 2017), we analyzed DKK3
103 protein in the soluble and insoluble fractions. Soluble DKK3 levels were increased in Braak I-
104 III patients when compared to control subjects (1.4-fold increase), but no changes were
105 observed in Braak IV-VI (**Figure 1B**). In the insoluble fraction, in contrast, DKK3 protein levels
106 were increased in Braak IV-VI (1.51-fold increase) (**Figure 1C**), which could be consistent with
107 the presence of DKK3 in Aβ plaques. To explore if DKK3 increases at early stages of AD, we
108 assessed DKK3 abundance in brain tissue from the dorsolateral prefrontal cortex using a
109 published proteomic study comprised of 106 controls, 182 AD cases, and 200 asymptomatic
110 AD cases (Johnson et al., 2022). The asymptomatic cases are at an early preclinical stage of
111 AD in which patients exhibit Aβ and tau pathology but no significant cognitive impairment (Jack
112 et al., 2018; Johnson et al., 2022). In line with our above results, DKK3 protein was elevated
113 in AD cases. Importantly, DKK3 was increased in asymptomatic AD cases and further
114 increased in AD cases when compared to asymptomatic AD (**Figure 1D**). Together, these
115 results demonstrate that DKK3 mRNA and DKK3 protein levels are elevated in the brains of
116 AD patients and increased with the progression of AD. Moreover, DKK3 protein is re-
117 distributed from soluble to insoluble fractions with disease progression.

118 **DKK3 accumulates at atrophic neurites around amyloid plaques in AD mouse models**

119 We next analyzed where DKK3 protein is present in healthy and AD mouse brains. *Dkk3* is
120 expressed in excitatory neurons in several brain areas including the hippocampus and
121 neocortex (Barrantes et al., 2006; Meister et al., 2015; Thompson et al., 2008). To study the
122 distribution of DKK3 protein, we used a specific DKK3 antibody, validated with brain samples
123 from total knockout *Dkk3*$^{-/-}$ mice by western blot (**Figure S1A**) and confocal microscopy
124 (**Figure S1B**). In the hippocampus, DKK3 protein was highly abundant in neurons of the CA1,
125 CA2, and CA3 pyramidal layers but not in the dentate gyrus (DG) granule cell layer (**Figure**
126 **S1C**), consistent with previous works studying *Dkk3* expression (Barrantes et al., 2006;
127 Thompson et al., 2008). In addition, DKK3 protein was present at lower levels in a subset of
128 astrocytes (GFAP-positive cells) (**Figure S1D**), but not in microglia (IBA1-positive cells)
129 (**Figure S1E**). Thus, principal neurons, followed by astrocytes, are the main source of DKK3
130 protein in the adult mouse hippocampus.

131 To further understand the role of DKK3 in the AD brain, we evaluated its localization within the
132 hippocampus of two AD mouse models when Aβ plaques are present. Aβ plaques are complex
133 structures closely associated with atrophic axons and dendrites of nearby neurons and with

134 glial cells (**Figure 2A**). Using confocal microscopy, we investigated the presence of DKK3 in
135 hippocampal Aβ plaques using anti-Aβ (6E10) in 18-month-old J20 (Mucke et al., 2000a) and
136 8-month-old hAPP$^{NL\text{-}G\text{-}F/NL\text{-}G\text{-}F}$ (NLGF) mice (Saito et al., 2014). DKK3 was present at Aβ
137 plaques in both AD lines (**Figure 2B and Figure S2A**). Furthermore, DKK3 was present in
138 both diffuse Aβ plaques (6E10-positive but ThioS negative) and dense-core plaques (positive
139 for 6E10 and ThioS) (**Figure S2B**). Importantly, 70% of dense-core Aβ plaques contained
140 DKK3 (**Figure 2C**). This localization was specific for DKK3, as other secreted proteins such
141 as Wnt7a/b did not localize to Aβ plaques (**Figure S2C**). Furthermore, DKK3 was absent from
142 astrocytes and microglia in Aβ plaques but specifically colocalized with Neurofilament-H+
143 dystrophic neurites (**Figure 2D & Figure S2D**). In addition, DKK3 also colocalized with LAMP1
144 in dystrophic neurites, which are visualized as axonal spheroids (**Figure 2D**). DAPI staining
145 further revealed that the deposition of DKK3 within amyloid plaques was not in cell body
146 inclusions (**Figure S2E**). Together, these results indicate that DKK3 is present in atrophic
147 neurites around amyloid plaques.

148 **Extracellular levels of DKK3 increase in the AD mouse brain through NMDAR activation**

149 The accumulation of DKK3 in Aβ plaques in AD and our finding that DKK3 protein is elevated
150 in the brain of AD patients (**Figure 1C&D**) led us to investigate whether DKK3 levels are
151 altered in the mouse AD brain. Given that DKK3 is a secreted protein, we examined total and
152 extracellular levels of DKK3 from acute hippocampal slices of wild-type (WT) and J20 mice at
153 3-4 months before plaques appear. Although the total DKK3 levels did not differ between J20
154 and WT mice in the brain homogenate, DKK3 levels were significantly increased (2.54-fold) in
155 the extracellular fraction of J20 mice (**Figure 2E**). In a second AD mouse model, NLGF,
156 extracellular DKK3 levels were also elevated by 2.43-fold in brain slices of these animals at 2-
157 3 months (**Figure 2F**). Importantly, the ratio of extracellular to total DKK3 levels was
158 significantly higher in J20 and NLGF when compared to their respective controls (**Figure**
159 **2E&F**), suggesting that DKK3 secretion is enhanced in AD mouse brains.

160 Our next studies focused on understanding the mechanisms underlying the extracellular
161 increase of DKK3 in AD mice. Mounting evidence demonstrates that Aβo trigger the
162 overactivation of *N*-methyl-D-aspartate (NMDA) receptors (NMDARs), which contributes to
163 long-term depression (LTD) in AD models (Li et al., 2011; Mucke and Selkoe, 2012). We
164 therefore investigated this question by using (2R)-amino-5-phosphonovaleric acid (APV) to
165 block NMDARs. APV completely prevented the increase of DKK3 in the extracellular fraction
166 of J20 and NLGF brain slices (**Figure 2E&F**). Given the increased levels of Aβ in these two
167 mouse models (Mucke et al., 2000a; Saito et al., 2014), we evaluated whether Aβ increases
168 DKK3 levels. We treated hippocampal neurons with Aβo ($A\beta_{1\text{-}42}$) or the reverse $A\beta_{42\text{-}1}$ control

169 peptide. Aβo increased DKK3 protein levels by 2.50- and 2.48-fold in the cellular lysate and
170 the extracellular fraction respectively (**Figure S2F-H**), indicating that Aβo increased the overall
171 levels of DKK3 in hippocampal neurons. Treatment of neurons with APV in the presence of
172 Aβo decreased extracellular DKK3 levels to 1.48-fold. Although this reduction did not reach
173 statistical significance using a Kruskal-Wallis with Dunn's test ($p = 0.0726$), it was statistically
174 significant using a t-test ($p = 0.0384$). These results suggest that blockade of NMDARs partially
175 occludes the ability of Aβo to increase DKK3 levels in the extracellular fraction.

176 Next, we examined whether DKK3 levels were regulated by NMDAR-mediated synaptic
177 plasticity by performing glycine-induced chemical long-term potentiation (cLTP) or NMDA-
178 induced chemical long-term depression (cLTD) in cultured hippocampal neurons. Induction of
179 cLTP did not affect DKK3 protein levels in the cellular or extracellular fractions (**Figure S3A**).
180 In contrast, cLTD significantly increased the levels of extracellular DKK3 without affecting the
181 levels in the cellular fractions (**Figure S3B**). Similar results were obtained using brain slices
182 after cLTD-induction (**Figure S3C**). To test if the increase in extracellular DKK3 was due to
183 changes in vesicular trafficking of DKK3, we used brefeldin A (BFA), which interrupts vesicle
184 trafficking and exocytosis (Brewer et al., 2022; He et al., 2015; Katsinelos et al., 2018). We
185 found that BFA treatment significantly reduced DKK3 levels in the extracellular space under
186 control conditions and completely prevented the increase in DKK3 levels following cLTD-
187 induction (**Figure S3C**). The lack of a difference in DKK3 levels in the total homogenate could
188 be explained by the fact that only a small fraction of cellular DKK3 is released into the
189 extracellular media, as supported by our findings that DKK3 was less abundant in the
190 extracellular fraction when compared to the total homogenate (**Figure S3D**). Together, these
191 results strongly suggest that trafficking/secretion of DKK3 was enhanced by NMDAR-
192 mediated cLTD-induction.

193 **DKK3 differentially affects excitatory and inhibitory synapses in the adult hippocampus**

194 Given that DKK1, a member of the Dkk family, leads to excitatory synapse disassembly and
195 synaptic plasticity defects (Galli et al., 2021, 2014; Marzo et al., 2016), we evaluated the
196 impact of increased DKK3 levels on synapses by performing *ex vivo* gain-of-function
197 experiments using brain slices (**Figure 3A**). We focused on the CA3 region as DKK3 is highly
198 expressed in this region (Thompson et al., 2008) (**Figure S1C**), and is required for encoding
199 spatial and other episodic memories, processes which are impaired in AD (Deuker et al.,
200 2014). Moreover, we previously reported that Aβo trigger synapse loss in the CA3 *stratum*
201 *radiatum* (SR) region of the hippocampus (Purro et al., 2012). Gain-of-function of DKK3
202 reduced the puncta number of the excitatory presynaptic marker vGLUT1 (by 38.99%), the
203 postsynaptic marker PSD-95 (by 32.58%), and the total number of excitatory synapses (by

204 60.85%), determined by the colocalization of these synaptic markers, in the CA3 SR (**Figure**
205 **3B**). These synaptic changes were not due to neuronal death (**Figure S4A&B**). Patch-clamp
206 recordings of CA3 neurons revealed that DKK3 gain-of-function decreased the frequency of
207 miniature excitatory postsynaptic currents (mEPSC) by 48.54% but did not affect their
208 amplitude (**Figure 3C**).

209 We further investigated whether DKK3 gain-of-function affects inhibitory synapses. DKK3
210 increased the density of puncta for the inhibitory postsynaptic marker gephyrin (by 55.39%)
211 without affecting the density of the inhibitory presynaptic marker vGAT in the CA3 SR (**Figure**
212 **3D**). Notably, DKK3 increased the number of inhibitory synapses (by 65.99%) (**Figure 3D**)
213 based on the colocalization of the pre and postsynaptic markers. Patch-clamp recordings of
214 CA3 neurons uncovered that DKK3 increased the frequency of miniature inhibitory
215 postsynaptic currents (mIPSC) by 65.56% but did not affect their amplitude (**Figure 3E**). In
216 the CA1 SR, DKK3 induced similar effects on excitatory and inhibitory synapse density (**Figure**
217 **S4C&D**). Together, these results demonstrate that DKK3 gain-of-function decreases
218 excitatory synapse number but increases inhibitory synapse number in the adult
219 hippocampus.

220 **DKK3 regulates excitatory synapse number through the Wnt/GSK3β pathway and**
221 **inhibitory synapse number through Wnt/JNK cascade**

222 We next examined the Wnt signaling pathways mediating DKK3-induced synaptic changes.
223 Wnts can signal through different pathways, including the Wnt/GSK3 and Wnt/JNK cascades
224 (Niehrs, 2012; Nusse and Clevers, 2017) (**Figure 4A&D**). A previous study showed that DKK1
225 induces synapse loss by blocking the canonical Wnt pathway in the hippocampus (Marzo et
226 al., 2016). To investigate if DKK3 triggers synaptic changes through this pathway, we
227 evaluated the puncta density of β-catenin, which is degraded upon inhibition of Wnt/GSK3β
228 signaling (Nusse and Clevers, 2017). To exclude changes in β-catenin density due to synapse
229 loss, we measured the density of extra-synaptic β-catenin as we had done before (Galli et al.,
230 2014). Indeed, DKK3 decreased the number of extra-synaptic β-catenin puncta in
231 hippocampal slices, which was restored when the Wnt/GSK3β cascade was activated using
232 the GSK3 inhibitor 6-bromoindirubin-3'-oxime (BIO) (Marzo et al., 2016) (**Figure 4B**).
233 Importantly, BIO increased the density of extra-synaptic β-catenin puncta under control
234 conditions, confirming the activation of canonical Wnt signaling (**Figure 4B**). We next explored
235 whether activation of canonical Wnt signaling prevented DKK3-induced synaptic changes. At
236 the concentration and time used, BIO did not affect the number of excitatory synapses under
237 control brain slices, but completely blocked the DKK3-induced loss of excitatory synapses
238 (**Figure 4C**). Similar results were obtained with CHIR99021, another highly specific GSK3

239 inhibitor (Ring et al., 2003) (**Figure S5A**). Thus, DKK3 affects excitatory synapse number
240 through the Wnt/GSK3β pathway.

241 Next, we investigated if DKK3 increases inhibitory synapses through canonical Wnt signaling
242 by blocking GSK3 using BIO. In contrast to excitatory synapses, BIO did not affect DKK3's
243 impact on inhibitory synapse density (**Figure S5B**). Therefore, DKK3 regulates inhibitory
244 synapse density independently of the Wnt/GSK3β pathway. Previous studies showed that
245 DKK1 concomitantly inhibits the Wnt/GSK3β pathway and activates the Wnt/Planar Cell
246 Polarity (PCP) signaling cascade (Caneparo et al., 2007; Killick et al., 2014; Marzo et al.,
247 2016). The PCP pathway activates c-Jun N-terminal kinase (JNK) (**Figure 4D**), which has
248 been implicated in Aβ toxicity (Killick et al., 2014). In brain slices, DKK3 increased phospho-
249 JNK, a readout for the JNK activation (**Figure 4E**). This increase was blocked by the JNK
250 inhibitor CC-930 (Plantevin Krenitsky et al., 2012) (**Figure 4E**), indicating that DKK3 activates
251 the Wnt/JNK signaling pathway. We next tested the effect of CC-930 on inhibitory synapses
252 and found that this JNK inhibitor blocked the DKK3-induced increase in the number of gephyrin
253 puncta and inhibitory synapse density (**Figure 4F**). In contrast, JNK inhibition did not block the
254 effect of DKK3 on excitatory synapses (**Figure S5C**). Together, our results indicate that DKK3
255 induces the loss of excitatory synapses through inhibition of Wnt/GSK3β signaling but
256 increases inhibitory synapses through activation of the Wnt/JNK pathway.

257 ***In vivo* DKK3 loss-of-function decreases inhibitory synapses without affecting**
258 **excitatory synapses in the healthy adult brain**

259 We next studied the *in vivo* role of DKK3 by downregulating DKK3 in adult WT mice using a
260 viral transduction approach. DKK3 was knocked down in the CA3 region of the hippocampus
261 using AAV9 expressing enhanced green fluorescent protein (EGFP) and scramble shRNA
262 (Scr shRNA) or shRNA against DKK3 (DKK3 shRNA) (**Figure 5A**), and synapses were
263 evaluated a month later. This approach led to approximately 85% knockdown of DKK3 at the
264 injection site (**Figure 5A**). Excitatory and inhibitory synapses were assessed by confocal
265 microscopy and by whole-cell patch-clamp recordings. In contrast to gain-of-function
266 experiments, DKK3 silencing did not affect excitatory synapse number (**Figure 5B**) or mEPSC
267 frequency (**Figure 5C**). However, DKK3 loss-of-function decreased the amplitude of mEPSCs
268 (by 28.18%, **Figure 5C**). Conversely, knockdown of DKK3 reduced the number of inhibitory
269 synapses (by 37.30%, **Figure 5D**), the frequency of mIPSCs (by 71.76%), and their amplitude
270 (by 35.02%, **Figure 5E**). Thus, downregulation of DKK3 in WT brain reduces the number of
271 inhibitory synapses without affecting excitatory synapses, suggesting that endogenous DKK3
272 is required for the maintenance of inhibitory synapses but not for the integrity of excitatory
273 synapses in the healthy adult brain.

274 ***In vivo* DKK3 loss-of-function ameliorates excitatory and inhibitory synapse changes**
275 **in J20 mice**

276 To investigate the contribution of DKK3 to synaptic changes in AD, we knocked down DKK3
277 in the hippocampus of J20 mice at two different disease stages using AAV9-Scr shRNA or
278 AAV9-DKK3 shRNA (**Figure 6A & Figure S6A**). J20 mice exhibit excitatory synapse loss in
279 the hippocampus at 4-months of age (early stage), whereas plaque deposition starts around
280 5-months and is widely distributed in the cortex and hippocampus by 9-months (late stage)
281 (Hong et al., 2016; Meilandt et al., 2009; Mucke et al., 2000a, 2000b). We first evaluated the
282 impact of DKK3 knockdown on excitatory and inhibitory synapses in J20 mice at early stages.
283 We found that 4-month-old J20 mice exhibited a 40-45% loss of excitatory synapses in the
284 CA3 SR when compared to WT (**Figure 6B & Figure S6B**) as previously reported (Hong et
285 al., 2016). Remarkably, DKK3 knockdown restored excitatory synapse number in J20 mice
286 (**Figure 6B & Figure S6B**). In contrast to excitatory synapses, inhibitory synapses were
287 increased by 20.60% in J20 mice compared to WT (**Figure 6C & Figure S6C**). Importantly,
288 DKK3 silencing decreased inhibitory synapse number in these mice (**Figure 6C & Figure**
289 **S6C**). Thus, *in vivo* DKK3 loss-of-function ameliorates synaptic defects in J20 mice, supporting
290 the hypothesis that DKK3 is a key contributor to synaptic changes in this AD mouse model.

291 A key feature of AD brains is the loss of synapses around Aβ plaques (Koffie et al., 2012).
292 Therefore, we investigated whether DKK3 affects synapse number around plaques in 9-
293 month-old J20 mice (**Figure 6A**). We observed a significant effect of distance on the density
294 of excitatory synapses from the core of the plaque ($F(6, 318) = 27.26$, p-value $< 0.0001$) and
295 inhibitory synapses ($F(6, 276) = 23.51$, p-value $< 0.0001$) (**Figure 6D&E**). Importantly, DKK3
296 silencing significantly increased the number of excitatory synapses (**Figure 6D & Figure S6D**)
297 but decreased the density of inhibitory synapses around plaques (**Figure 6E & Figure S6E**)
298 when compared to J20 mice injected with Scr shRNA. Importantly, knockdown of DKK3 did
299 not affect the number or size of plaques in the CA3 SR (**Figure S6F**).

300 Given the role of DKK1 in synaptic changes and in AD (Caricasole et al., 2004; Marzo et al.,
301 2016; Purro et al., 2012), we next investigated whether modulation of DKK3 levels affected
302 *Dkk1* mRNA levels in the hippocampus of WT and J20 mice injected with Scr or DKK3 shRNA.
303 However, no changes in *Dkk1* mRNA levels were observed (**Figure S6G**). We next
304 investigated whether increased *Dkk1* led to changes in *Dkk3* expression. For this, we used a
305 transgenic mouse model that expresses *Dkk1* upon induction (*iDkk1* mice) (Galli et al., 2021,
306 2014; Marzo et al., 2016). After 14 days of *Dkk1* expression and when synaptic changes are
307 observed in these mice, we found that *Dkk3* levels were unaltered in the hippocampus (**Figure**
308 **S6H**). Thus, *Dkk3*'s expression is unaffected by *Dkk1* and vice versa. Together, these results

309 demonstrate that loss-of-function of DKK3 ameliorates excitatory and inhibitory synapse
310 changes in J20 mice independently of DKK1 before plaque burden starts (4-months-old), and
311 later when amyloid plaque pathology is evident (9-months-old).

312 ***In vivo* DKK3 loss-of-function improves memory in J20 mice**

313 The finding that DKK3 loss-of-function reverses synaptic changes at early and late stages in
314 J20 mice led us to test whether silencing DKK3 restores hippocampal-mediated learning and
315 memory in these mice (**Figure 7A**). Knockdown of DKK3 using viral injections did not affect
316 exploratory activity or anxiety in J20 mice (**Figure S7A&B**). In contrast, DKK3 downregulation
317 significantly improved spatial memory in J20 mice as evaluated by the novel object location
318 test (NOLT) (**Figure 7B**). Next, we examined long-term spatial working memory using the
319 Morris Water Maze (MWM). No deficiencies in vision or locomotion were observed as escape
320 latencies did not differ between groups when the platform was visible (**Figure S7C**). We then
321 assessed reference spatial learning using the hidden platform version of the MWM (**Figure**
322 **7C**). Performance improved significantly in all 4 groups during training, although the escape
323 latency in J20-Scr shRNA mice remained significantly higher than that of WT-Scr shRNA mice
324 (**Figure 7C**). Importantly, silencing DKK3 in J20 mice fully rescued this defect (**Figure 7C**). To
325 test spatial memory, probe trials were performed on day 5 (early probe) and day 8 (late probe).
326 In the first early probe test, J20-Scr shRNA animals traveled significantly less in the target
327 quadrant than WT-Scr shRNA mice (**Figure 7D**). After further training, in the late probe, the
328 time to first entrance to the target location (platform) and the distance traveled in the target
329 quadrant were restored in the J20-DKK3 shRNA mice when compared to J20-Scr shRNA mice
330 (**Figure 7E**). Together, these results demonstrate that DKK3 downregulation in the
331 hippocampus restores cognitive function in J20 AD mice. In summary, our functional studies
332 in mice together with our results obtained from human AD patients strongly support a role for
333 DKK3 in synapse dysfunction and memory impairment in AD.

334 **DISCUSSION**

335 Synapse loss is the strongest correlate with cognitive impairment in AD (Mucke and Selkoe,
336 2012; Selkoe and Hardy, 2016). However, the mechanisms that trigger synaptic changes
337 remain poorly understood. In this work, we investigated the function of the Wnt antagonist
338 DKK3 on synaptic integrity and memory in the healthy and AD brain. Our functional analyses
339 in AD models and our studies in human samples strongly support the notion that DKK3
340 contributes to synapse defects and memory impairment in AD.

341 Our analyses of brain samples from AD patients show an upregulation of DKK3 at the mRNA
342 and protein levels. Importantly, DKK3 elevation starts from early stages as we observed
343 increased protein levels in Braak I-III subjects and in asymptomatic cases using a published
344 proteomic dataset (Johnson et al., 2022). These findings are in agreement with other
345 proteomic studies showing increased levels of DKK3 in different brain areas, including the
346 hippocampus and in cortical synaptosomes of AD patients (Hesse et al., 2019; Xu et al., 2019).
347 Together, our findings in AD patients suggest that increased DKK3 levels in the brain could
348 underlie synapse dysfunction in AD.

349 Amyloid plaques are a prominent neuropathological feature of AD. A previous study revealed
350 that DKK3 is present at Aβ plaques in the brains of AD subjects (Bruggink et al., 2015), which
351 was later confirmed by proteomic studies in human and mouse brains (Drummond et al., 2017;
352 Xiong et al., 2019). Consistent with these findings, we demonstrate that DKK3 accumulates at
353 both diffuse and dense-core Aβ plaques in two AD mouse models: the NLGF and J20 lines.
354 Moreover, our analyses revealed that DKK3 is specifically localized at axonal spheroids. DKK3
355 colocalized with LAMP1, suggesting that DKK3 is present in abnormally enlarged vesicles.
356 This accumulation could indicate changes in DKK3 transport within dystrophic neurites
357 affecting its degradation and/or secretion. We found that extracellular DKK3 levels are
358 elevated in brain slices from J20 and NLGF models before substantial amyloid burden occurs,
359 whereas acute exposure to Aβo increase both total and extracellular DKK3 levels in neurons.
360 Intriguingly, a study reported reduced levels of DKK3 in the human AD brain and an AD mouse
361 model (Zhang et al., 2017), but the specificity of the DKK3 antibody used in this study was not
362 demonstrated. Moreover, this work indicated that overexpression of DKK3 restored memory
363 in an AD model (Zhang et al., 2017). However, the generation of these mice was not fully
364 characterized. Importantly, this study is in disagreement with other human proteomic studies
365 (Hesse et al., 2019; Johnson et al., 2022; Xu et al., 2019) and our own findings that DKK3 is
366 elevated in AD. Indeed, our studies using a validated antibody revealed that DKK3 is elevated
367 in the brains of AD patients. In conclusion, our results are consistent with several other findings
368 that DKK3 levels are increased in AD suggesting that elevated DKK3 may contribute to AD
369 pathogenesis.

370 How are DKK3 levels regulated? Here we demonstrate that activity-dependent modulation of
371 NMDARs regulates DKK3 levels. Several studies showed that Aβo block glutamate uptake by
372 neurons, raising the extracellular glutamate levels and aberrantly activating NMDARs, leading
373 to impaired synaptic function and memory (Li et al., 2011; Mucke and Selkoe, 2012).
374 Furthermore, blockade of NMDARs protects synapse density and cognitive function in AD
375 mouse models (Hu et al., 2009; Ye et al., 2004). Our studies revealed that the increased

extracellular DKK3 levels in the hippocampus of J20 and NLGF mice are completely abolished by blockade of NMDARs. Conversely, extracellular DKK3 levels are increased by NMDAR-induced cLTD without affecting total levels of the protein. These apparently paradoxical results could be reconciled by our finding that only a small proportion of DKK3 is released from neurons, and therefore changes in DKK3 protein levels are not detected in the total cell lysate. These findings suggest that overactivation of NMDARs may trigger DKK3 release. Consistent with this suggestion, treatment with BFA, an inhibitor of vesicle transport used to study the release of proteins (Brewer et al., 2022; He et al., 2015; Katsinelos et al., 2018), blocks the increase in extracellular levels of DKK3 after cLTD. Given that LTD is increased in AD, these results suggest a possible mechanism for the regulation of DKK3 secretion in this condition.

DKK3 is the most highly expressed member of the DKK family of Wnt antagonists in the human and mouse brain (Zhang et al., 2014). Here, we demonstrate a novel role for DKK3 in differentially regulating both excitatory and inhibitory synapses in the hippocampus. These results are in contrast to those obtained with DKK1, which only affects excitatory synapses in the hippocampus (Marzo et al., 2016). Indeed, gain-of-function of DKK3 decreases the number of excitatory synapses but increases inhibitory synapses in the adult hippocampus. Conversely, *in vivo* knockdown of endogenous DKK3 in adult WT mice decreases inhibitory synapses but does not affect excitatory synapse density. This finding suggests that other molecules might compensate for the loss of DKK3 resulting in the maintenance of excitatory synapse number under basal conditions in the healthy brain. However, knockdown of DKK3 reduces the amplitude of mESPCs. A possible explanation for this finding is that endogenous DKK3 is required for excitatory synapse function without affecting their structural stability.

Our results also demonstrate that DKK3 signals through different pathways to regulate excitatory and inhibitory synapses. A key component of the canonical Wnt pathway is GSK3β. The activity of GSK3β is increased in the AD brain, which is associated with reduced Wnt signalling (Leroy et al., 2007). Importantly, activation of canonical Wnt pathway by inhibition of GSK3 blocks DKK3-mediated excitatory synapse loss, which is consistent with a role for DKK3 as an antagonist of canonical Wnt signaling (Caricasole et al., 2003; Mizobuchi et al., 2008; Zhu et al., 2014). GSK3β also plays a role in the production of mitochondrial ATP, a key event in maintaining synapses (Gomez-Suaga et al., 2022). However, this function is disrupted in the presence of toxic proteins such as Tau and, importantly, recovered by inhibition of GSK3β (Gomez-Suaga et al., 2022; Szabo et al., 2023). Thus, DKK3 could also contribute to the loss of excitatory synapses by impairing mitochondrial function through activation of GSK3β.

410 In contrast to excitatory synapses, blockade of GSK3 does not restore the impact of DKK3 on
411 inhibitory synapse number. Instead, JNK blockade prevents DKK3-induced inhibitory synapse
412 assembly, indicating a role for Wnt/JNK signaling in this process. Our finding that DKK3
413 activates JNK in the hippocampus is consistent with previous results in other cell types
414 (Abarzua et al., 2005; Mizobuchi et al., 2008; Yu et al., 2017). Importantly, JNK blockade did
415 not affect the loss of excitatory synapses by DKK3. Together, our results show that DKK3
416 regulates the stability of excitatory and inhibitory synapses in the adult hippocampus through
417 different signaling pathways.

418 Our functional studies in the J20 mouse model of AD demonstrate that knocking down DKK3
419 in J20 mice ameliorates the changes in excitatory and inhibitory synapse number in the
420 hippocampus both before and after plaque deposition. Although loss of synapses around
421 amyloid plaques is well described (Koffie et al., 2012), changes in synapse number induced
422 by silencing DKK3 is unlikely to be due to the formation of plaques as we observed similar
423 synaptic changes when plaques are absent. In line with this view, knockdown of DKK3 does
424 not affect the number or size of amyloid plaques in the J20 hippocampus. Moreover, our gain-
425 of-function studies demonstrate that DKK3 directly affects the integrity of excitatory and
426 inhibitory synapses. Crucially, downregulation of DKK3 also improves cognitive function,
427 particularly spatial memory, in J20 mice. The rescue of the synaptic and cognitive defects is
428 specific to DKK3 downregulation as no differences in *Dkk1* levels, a Wnt antagonist that affects
429 synapses (Marzo et al., 2016), are observed.

430 Our functional studies in the J20 demonstrate a novel role for DKK3 in synaptic and cognitive
431 function. In addition, our results using human AD brain samples provide strong support for the
432 contribution of DKK3 to AD. Thus, DKK3 is a potential target for ameliorating excitatory and
433 inhibitory synaptic impairment and memory dysfunction in AD.

434 **MATERIALS AND METHODS**

435 **Human tissue**

436 Anonymized human samples from control and AD patients were obtained from Cambridge
437 Brain Bank (CBB), Division of the Human Research Tissue Bank, Addenbrooke's Hospital,
438 Cambridge, UK. All samples were obtained with informed consent under CBB license (NRES
439 10/HO308/56) approved by the NHS Research Ethics Services. Tissues were stored at -80°C.
440 Demographic data and Braak stages for each subject are shown in **Table S1**.

441 **Mice**

442 All procedures involving animals were conducted according to the Animals Scientific
443 Procedures Act UK (1986) and in compliance with the ethical standards at University College
444 London (UCL). WT C57BL/6J were obtained from Jackson Laboratories. J20 mice were
445 obtained from Jackson Laboratories and maintained on a C57BL/6J genetic background. J20
446 hemizygous transgenic males were bred with WT C57BL/6J females to generate hemizygous
447 transgenic mice (J20) and WT littermates. Genotyping was performed using DNA from ear
448 biopsies and with the following primers to detect the human APP transgene: forward 5'-
449 GGTGAGTTTGTAAGTGATGCC-3' and reverse 5'- TCTTCTTCTTCCACCTCAGC -3'. $APP^{NL-G-F/NL-G-F}$
450 mice were obtained from Saito et al. (Saito et al., 2014) and maintained in C57BL/6J
451 background as previously described (Palomer et al., 2022). Double transgenic mice (i*Dkk1*)
452 were obtained by crossing tetO-Dkk1 transgenic mice with CaMKIIαrtTA2 transgenic mice
453 (both C57BL/6J background) as previously described (Galli et al., 2014; Marzo et al., 2016).
454 Adult control (tetO-Dkk1, CaMKIIα-rtTA2 or wild-type littermates) and i*Dkk1* mice were fed
455 with food pellets containing 6mg/kg doxycycline for 14 days. Animals were housed in
456 ventilated cages with access to food and water ad libitum and kept at 22±2°C and 55±10%
457 humidity with a 12h/12h light cycle. Experimental animals included males and females. The
458 ages of mice are specified in each figure legend, according to the experimental approach
459 used.

460 **Primary hippocampal cultures treatments**

461 Primary hippocampal neurons (700 cells/$mm^2$) were isolated from embryonic day 18 Sprague-
462 Dawley rat embryos and cultured on poly-L-lysine coated plates or glass coverslips in
463 Neurobasal medium containing N2 and B27 supplements (Invitrogen). Neurons were
464 maintained in a 5% $CO_2$ humidified atmosphere at 37ºC. One-third of the media was
465 replenished every seven days. All experiments were performed at 20-21 days-in-vitro (DIV).

466 ***Aβ oligomers (Aβo) preparation***

467 Synthetic Aβ ($A\beta_{1-42}$) or reverse Aβ ($A\beta_{42-1}$) peptides were prepared as previously described
468 (Purro et al., 2012) with minor modifications. Briefly, HFIP films of $A\beta_{42-1}$ (Bachem, Cat#
469 4107743) and $A\beta_{1-42}$ (Bachem, Cat# 4090148) were dissolved in DMSO to a concentration of
470 5 mM. The solution was then sonicated at 40Hz for 10 minutes followed by vortexing for 30
471 seconds. Sterile PBS was added to achieve a final $A\beta_{1-42}$ or $A\beta_{42-1}$ concentration of 100 μM,
472 and vortexed again for 20 seconds. The peptides were left to oligomerize for 24 hours at 4°C.
473 Oligomeric preparations were centrifuged for 10 minutes at 14,000g and the solution was
474 collected. Aggregation into oligomers was evaluated by native PAGE. 30μl of Aβ preparations
475 were loaded into a 16% polyacrylamide gel and transferred onto a nitrocellulose membrane.
476 Membranes were boiled for 5 minutes in TBS, blocked with 10% non-fat milk for 60 minutes
477 at room temperature, and incubated with anti-Aβ antibody (6E10) O/N at 4°C. 19-21DIV
478 dissociated hippocampal neurons were treated with 200 nM $A\beta_{1-42}$ (monomers, dimers,
479 trimers, and tetramers) or reverse $A\beta_{42-1}$ control for 3 hours at 37 °C in combination with APV
480 (20 μM) or vehicle (PBS). Neurons were pre-treated with APV or vehicle 30 minutes prior to
481 co-treatment with Aβ and APV.

482 ***Chemical LTP and chemical LTD***

483 Hippocampal neurons were subjected to cLTP or cLTD induction at 21DIV using glycine
484 (McLeod et al., 2018) or NMDA (Kamal et al., 1999) respectively. Briefly, 200 μM glycine
485 (Fisher Chemical) or 20 μM NMDA (Tocris Bioscience), or the vehicle PBS, were applied to
486 cultures for 10 or 5 minutes respectively. The media was then replaced with fresh medium.
487 Lysates from neurons and extracellular media were processed for Western Blot analyses after
488 15 minutes of exposure to DMSO, NMDA or glycine. Levels of phospho-GluA1 Ser845 and
489 total GluA1 were evaluated as readouts.

490 **Hippocampal stereotactic surgery**

491 Stereotactic injection of AAV9-EGFP-U6-Scramble shRNA or AAV9-EGFP-U6-DKK3 shRNA
492 (both from VectorLabs) was performed bilaterally in the CA3 area of the hippocampus. The
493 sequence for Scr shRNA and DKK3 shRNA were as follows: Scr shRNA, 5'-
494 CCTAAGGTTAAGTCGCCCTCGCTCGAGCGAGGGCGACTTAACCTTAGGTTTTT-3' and
495 DKK3 shRNA, 5'-
496 GAGCCATGAATGTATCATTGACTCGAGTCAATGATACATTCATGGCTCTTTTT-3'. Adult
497 mice were deeply anesthetized using a mixture of oxygen and isoflurane (4% for induction and
498 2-1% for maintaining anaesthesia). Using a stereotactic frame, two injections were performed

499 in the hippocampus at the following coordinates relative to bregma [anteroposterior (AP) and
500 mediolateral (ML) and to dural surface (dorsoventral (DV): (1) -1.7AP, ±2 ML, -1.85 DV; (2) -
501 2.3 AP, ±2.8 ML, -2.2 DV. Viral particles were injected into the brain using a 10µl Hamilton
502 microliter syringe at an infusion rate of 100nl/min. The needle was left for 5 additional minutes
503 to ensure diffusion of the virus, then slowly retracted from the brain. After 4 weeks, synapses,
504 behavior or gene expression were evaluated.

505 **Treatment of acute hippocampal slices**

506 WT and J20 mouse brains were rapidly dissected and placed in 5% $CO_2$/95% $O_2$ ice-cold
507 aCSF containing (in mM): 87 NaCl, 2.5 KCL, 25 $NaHCO_3$, 1.25 $Na_2HPO_4$, 0.5 $CaCl_2$, 7 $MgCl_2$,
508 10 D-(+)-Glucose, 75 sucrose (pH = 7.4). Sagittal 300 µm slices were obtained with a
509 vibratome and transferred to 5% $CO_2$/95% $O_2$ aCSF (34ºC) containing (in mM): 125 NaCl, 2.5
510 KCL, 25 $NaHCO_3$, 1.25 $Na_2HPO_4$, 1 $CaCl_2$, 2 $MgCl_2$, 25 D-(+)-Glucose (pH = 7.4). Brain slices
511 were maintained in warm aCSF solution for 60 min before starting treatments.

512 Brain slices were treated with 150 ng/ml recombinant DKK3 (R&D systems) or vehicle control
513 (PBS) for 4h (for synapse density evaluation) or 60 minutes (for phospho-JNK levels) or 200
514 ng/ml for 3h (for electrophysiological recordings). Drugs used include 0.5 µM BIO
515 (Calbiochem) or vehicle (DMSO); 60 nM CC-930 (Cayman Chemical) or vehicle (DMSO); 1µM
516 CHIR99021 (Calbiochem) or vehicle (DMSO); 20 µM NMDA (Tocris Bioscience) or vehicle
517 (PBS); 50 µM APV (Tocris Bioscience) or vehicle (PBS); 10 µg/ml Brefeldin A (Biolegend) or
518 vehicle (DMSO).

519 **Electrophysiology**

520 Transverse hippocampal slices (300µm) were cut on a vibratome in ice-cold aCSF bubbled
521 with 95% $O_2$ /5% $CO_2$ containing (in mM): 125 NaCl, 2.4 KCl, 26 $NaHCO_3$, 1.4 $NaH_2PO_4$, 20
522 D-(+)-Glucose, 0.5 $CaCl_2$ and 3 $MgCl_2$ as previously described (Redlingshöfer et al., 2020).
523 CA3 pyramidal neurons were patched in whole-cell voltage-clamp configuration using pipettes
524 (resistance 5–8 MΩ) pulled from borosilicate glass and filled with caesium gluconate
525 intracellular solution containing (in mM): 130 D-gluconic acid lactone, 10 Hepes, 10 EGTA, 10
526 NaCl, 0.5 $CaCl_2$, 1 $MgCl_2$, 1 ATP and 0.5 GTP, 5 QX314 (pH to 7.2 with CsOH). Slices were
527 perfused with the same aCSF solution as before except substituted with 1mM $MgCl_2$ and 2mM
528 $CaCl_2$. All miniature currents were recorded in the presence of 100nM TTX (Abcam). mEPSCs
529 were held at -60 mV with 10 µM bicuculline (Tocris Bioscience) and 50 µM APV (Tocris
530 Bioscience) added, whereas mIPSCs were held at 0 mV in the presence of 50 µM APV (Ciani
531 et al., 2011). Currents were recorded using an Axopatch 200B amplifier and low pass filtered

532 at 1 kHz and digitized (10 kHz). Analyses were performed using a combination of WinEDR
533 and WinWCP (available free online at
534 http://spider.science.strath.ac.uk/sipbs/software_ses.htm) software. For event detection, the
535 "template" function in WinEDR software was used (Clements and Bekkers, 1997). Several
536 filters were applied to exclude events that were unlikely to be genuine.

537 **Tissue processing for immunofluorescence microscopy**

538 Acute slices (300 µm) were fixed in 4% paraformaldehyde (PFA)/4% sucrose for 20 minutes.
539 Brains used for obtaining cryosection slices were fixed overnight in 4% PFA followed by
540 cryopreservation in 30% sucrose before freezing. Free-floating sagittal hippocampal sections
541 (30 µm) were obtained using a Leica cryostat.

542 Immunofluorescence staining of brain slices was performed as previously described (Marzo
543 et al., 2016; McLeod et al., 2018). Briefly, slices were permeabilized and blocked using 10%
544 donkey serum and 0.3% (for cryosections) or 0.5% (for acute slices) Triton X-100 in PBS for
545 3-5 hours at room temperature. Slices were then incubated with primary antibody overnight at
546 4ºC, followed by secondary antibody incubation (Alexa Fluor, 1:600, Invitrogen) for 2 hours at
547 room temperature and DAPI (1:50,000, Invitrogen) staining for 10 min to counterstain nuclei.
548 Thioflavin S (ThioS, Invitrogen) staining was performed as previously described (Ly et al.,
549 2011). Briefly, after incubation with secondary antibodies (1:500-1:600, Alexa Fluor, Thermo
550 Fisher Scientific or Jackson ImmunoResearch Labs), brain slices were dehydrated and
551 incubated with 1% ThioS for 15 min. Slices were then rehydrated and washed in water. Brain
552 slices were mounted with Fluoromount-G (Southern Biotech). TUNEL (Abcam) assay was
553 performed following manufacturer's instructions.

554 Primary antibodies and dilutions used for immunofluorescence were: mouse Anti- Aβ (6E10
555 clone, 1:1,000, Biolegend, Cat# 803001, RRID:AB_2564653), Rabbit Anti-Aβ (6E10 clone,
556 chimeric, 1:1,000, Novus Biologicals, Cat# NBP2-62566, RRID:AB_2917960), chicken anti-
557 Bassoon (1:1,000, Synaptic Systems, Cat# 141 016, RRID:AB_2661779), Goat anti- Mouse
558 DKK-3 (1:1,000, R and D Systems, Cat# AF948, RRID:AB_355734), Rabbit anti-Gephyrin
559 (1:500, Synaptic Systems, Cat# 147 002, RRID:AB_2619838), Chicken anti-Glial Fibrillary
560 Acidic Protein (GFAP) (1:500, Millipore, Cat# AB5541, RRID:AB_177521), Rabbit anti-
561 Homer1 (1:1,000, Synaptic Systems, Cat# 160 003, RRID:AB_887730), chicken Anti-GFP
562 (1:500, Millipore, Cat# 06-896, RRID:AB_310288), rabbit anti-Iba1 (1:1,000, FUJIFILM Wako
563 Shibayagi, Cat# 019-1974,1 RRID:AB_839504), rat anti-LAMP1 (1:250, DSHB, 1D4B,
564 RRID:AB_528127), rabbit Anti-NeuN (D3S3I) (1:1,000, Cell Signaling Technology, Cat#
565 12943, RRID:AB_2630395), rabbit Anti-Neurofilament Heavy (1:5,000, Abcam, Cat# ab8135,

566 RRID:AB_306298), mouse Anti-PSD-95 (7E3-1B8) (1:500, Thermo Fisher Scientific, Cat#
567 MA1-046, RRID:AB_2092361), guinea pig anti-vesicular GABA Transporter (vGAT) (1:500,
568 Synaptic Systems, Cat# 131 004, RRID:AB_887873), guinea pig Anti-Vesicular Glutamate
569 Transporter 1 (vGLUT1) (1:2,000, Millipore, Cat# AB5905, RRID:AB_2301751), goat anti-
570 Wnt7a/b (1:1,000, R&D Systems, Cat# AF3460, RRID:AB_2304437), mouse Anti- beta
571 Catenin (1:1,000, BD Biosciences, Cat# 610153, RRID:AB_397554).

572 **Image acquisition and analyses**

573 Confocal images were acquired using a Leica SP8 microscope and analyzed using ImageJ-
574 FIJI (NIH) or Volocity 3D Image Analysis version 6.5.1 (Quorum Technologies). For analyses
575 of synaptic puncta, 3 images from at least 3 brain sections per animal or 8-12 images from 2-
576 3 separate coverslips per culture were acquired using a 63X (1.40 Numerical Aperture (NA))
577 oil objective. Each image comprised 8 equidistant planes (0.3 µm apart) of 76nm x 76nm. To
578 analyze synapse density around a plaque, the plaque core was identified (core) and synapse
579 number per 200 $\mu m^3$ was quantified at each distance from the plaque core. The number of
580 pre- and post-synaptic puncta and number of synapses assessed as colocalization of pre- and
581 post-synaptic markers was quantified using Volocity imaging software as previously described
582 (Galli et al., 2014; Marzo et al., 2016; McLeod et al., 2017). Each independent value was
583 obtained from the average of each brain section (unless otherwise stated) and the data were
584 presented as relative values to the control and depicted as a percentage. For evaluating DKK3
585 in 6E10 plaques of J20 and NLGF mice, images from the whole hippocampus were obtained
586 with a tile scan using a 20X (0.75 NA) objective. Each stack comprised 30 equidistant planes
587 1 µm apart. Plaque quantification was performed using ImageJ-FIJI as previously described
588 (Jones et al., 2023). Images from the CA3 SR were thresholded, and the particle analysis tool
589 was used to obtain the number and size of plaques and the percent coverage area of Aβ. For
590 assessing DKK3 localization in ThioS positive plaques in the J20 brain, hippocampal images
591 from at least 3 brain sections per animal were acquired using a 20X (0.75 NA) objective. Each
592 image comprised 21 equidistant planes 50 nm apart. Presence of DKK3 in plaques was
593 evaluated manually, and the average of the different brain slices per mouse was obtained.
594 Data were displayed as values relative to the control condition and depicted as a percentage.
595 For evaluating the colocalization of DKK3 with different components of Aβ plaques, at least 3
596 plaques from 3-4 brain sections per animal were obtained using a 63X (1.40 NA) oil objective.
597 Each image comprised 8 equidistant planes (0.3 µm apart). Colocalization analyses of DKK3
598 and other markers (MAP2, Neurofilament H, IBA1, or GFAP) were performed in Volocity
599 software using Pearson´s coefficient tool based on intensity threshold values (the same
600 threshold was used for all images). To assess DKK3 intensity in the CA3 area, 3 images from

601 3 brain slices per animal were taken using a 20X (14 equidistant planes 2.41 µm apart) or a
602 40X (8 equidistant planes 0.3 µm apart) oil objective. For each image, DKK3 intensity was
603 normalized to MAP2 intensity using Volocity. The number of animals or independent cultures
604 are indicated in the figure legends.

605 **Protein extraction and Western blot**

606 Proteins were extracted from WT and J20 hippocampi, primary hippocampal neurons, or
607 human hippocampus with RIPA buffer (10mM Tris, 100mM NaCl, 1mM EDTA, 1% Nonidet P-
608 40, 0.1% SDS, 0.5% deoxycholate, pH = 8). Samples were then sonicated and centrifuged at
609 14,000g for 10 minutes at 4ºC. The supernatant representing the soluble protein fraction was
610 collected. For human brain samples, the pellet was washed in RIPA buffer and solubilized in
611 4% SDS. Thereafter, samples were sonicated and centrifuged at 14,000g for 10 minutes at
612 4ºC to obtain the SDS-soluble fraction (insoluble protein fraction).

613 To evaluate the extracellular fraction of cultured neurons or brain slices, cell media from
614 primary neurons and aCSF from acute slices treatments were collected and centrifuged at
615 14,000g for 10 minutes at 4ºC to evaluate extracellular levels of DKK3.

616 Protein concentration for all samples was quantified using a BCA kit (Thermo Fisher Scientific)
617 according to the manufacturer's protocol. Protein extracts were resolved on 10% SDS-PAGE
618 gels. Membranes (PVDF) were blocked with 5% non-fat milk and incubated with primary
619 antibodies overnight at 4ºC, followed by incubation of secondary antibodies for 60 min at room
620 temperature. Chemiluminescent images were acquired using ChemiDoc and fluorescent
621 images (total JNK) were obtained using LiCor Odissey Clx. All images were quantified by
622 densitometric analysis using ImageJ.

623 Primary antibodies and dilutions used for western blot were: Mouse Anti- Aβ (6E10 clone,
624 1:1,000, Biolegend, Cat# 803001, RRID:AB_2564653), goat anti- Mouse DKK-3 (1:1,000,
625 R&D Systems, Cat# AF948, RRID:AB_355734), goat anti- Human DKK-3 (1:1,000, R&D
626 Systems, Cat# AF1118, RRID:AB_354610), rabbit anti-GAPDH (1:5,000, Abcam, Cat#
627 ab181602, RRID:AB_2630358), rabbit anti-GluA1 (1:1,000, Cell Signaling Technology, Cat#
628 13185, RRID: AB_2732897), rabbit anti-phospho GluA1 Serine 845 (1:1,000, Cell Signaling
629 Technology, Cat# 8084, RRID: AB_10860773), rabbit anti- SAPK/JNK (1:1,000, Cell Signaling
630 Technology, Cat# 9252, RRID:AB_2250373), mouse anti-Phospho-SAPK/JNK
631 (Thr183/Tyr185) (1:500, Cell Signaling Technology, Cat# 9255, RRID:AB_2307321), mouse
632 anti-Tubulin (1:5,000, Sigma-Aldrich, Cat# T9026, RRID:AB_477593), mouse Anti-Vinculin

633 (1:2,000, Sigma Aldrich, Cat# v4505, RRID: AB_477617), HRP mouse anti-beta Actin
634 (1:10,000, Abcam, Cat# ab8224, RRID:AB_449644).

635 Secondary antibodies and the dilutions used for western blot were: Donkey anti-goat IgG-HRP
636 (1:2,000, Santa Cruz Biotechnology, Cat# sc-2020, RRID:AB_631728), donkey anti-goat IgG-
637 HRP (1:10,000, R&D Systems, Cat# HAF109, RRID:AB_357236), Sheep anti-Mouse IgG-
638 HRP (1:3,000, GE Healthcare, Cat# NXA931, RRID:AB_772209), donkey anti-Rabbit IgG-
639 HRP (1:2,000, GE Healthcare, Cat# NA934, RRID:AB_772206), goat anti-Rabbit IgG
640 IRDeye® 800CW (1:10,000, Abcam, Cat# ab216773, RRID:AB_2925189).

641 **Western blot analyses**

642 Chemiluminescent and fluorescent images from western blot membranes were acquired using
643 ChemiDoc (BioRad) or Odissey Clx (LiCor) respectively. DKK3 chemiluminescent signals from
644 total homogenates or cell lysates were obtained within seconds (0.5-15 seconds), whereas
645 extracellular signals were obtained within minutes (1-5 minutes). Blots were quantified by
646 densitometric analyses using ImageJ. Densitometric target signals were normalized to the
647 loading control signal (except for extracellular levels) and depicted as relative levels. The ratio
648 of extracellular/lysate DKK3 was obtained by dividing the normalized values of DKK3 in the
649 extracellular fraction by the values of the lysate for each condition. For quantification of P-JNK,
650 densiometric quantification of P-JNK was corrected for the densitometric signal of total JNK.

651 **RNA extraction, reverse transcription and quantitative PCR (qPCR) analyses**

652 RNA was extracted from the hippocampus of WT, J20, and i*Dkk*1 mice using TRIzol (Thermo
653 Fisher Scientific) and the DirectZol RNA MiniPrep Kit (Zymo Research), following the
654 manufacturer's instructions and as previously described (Palomer et al., 2022).
655 Retrotranscription to first-strand cDNA was performed using the RevertAid H Minus First
656 Strand cDNA Synthesis kit (Thermo Fisher Scientific) as per manufacturer's instructions. 5-30
657 ng of the original RNA was used to perform qPCR for *Dkk3* and *Dkk1* using GoTaq qPCR
658 Master Mix (Promega) in a CFX96 Bio-rad system following the manufacturer's protocol (2
659 min at 95°C followed by 40 cycles of denaturing at 95°C and annealing/extension at 60°C).
660 *GusB*, *Pgk1,* and *Rpl13a* were used as housekeeping genes. All primers were purchased from
661 Sigma-Aldrich and used at a final concentration of 0.5 µM. The following primers were used:
662 *Dkk1 (forward:* 5'-CCGGGAACTACTGCAAAAAT-3'; reverse: 5'-
663 AAAATGGCTGTGGTCAGAGG-3'), *Dkk3* (forward*:* 5'- GACCAGGGTGGGAAATAACA-3';
664 reverse: 5'-GACCACCTGTCCACTCTGGT-3'), *GusB* (forward: 5'-
665 GGTTTCGAGCAGCAATGGTA-3'; reverse: 5'-GCTGCTTCTTGGGTGATGTC-3'), *Pgk1*

666 (forward: 5'-TACCTGCTGGCTGGATGG-3'; reverse: 5'-CACAGCCTCGGCATATTTCT-3'),
667 *Rpl13a* (forward: 5'-GACTCCTGGTGTGAACCCA-3'; reverse: 5'-
668 CTCTACCCACAGGAGCAGT-3').

669 Relative expressions of *Dkk1* and *Dkk3* mRNAs were calculated using the comparative
670 threshold cycle (Ct) method. Samples were run in triplicate and the average Ct values were
671 obtained using the CFX Manager software version 3.1 (BioRad). Gene expression was
672 normalized to the expression of housekeeping genes.

673 **Behavioral tests**

674 Two separate cohorts of 4-month-old WT and J20 mice injected with Scr or DKK3 shRNA
675 were used to perform behavioral tests. All tests were carried out in a dimly lit room without
676 noise interference. Animals were tracked using the automated SMART video tracking software
677 (Panlab).

678 ***Elevated plus maze***

679 Anxiety was tested using an elevated plus maze consisting of four arms (30.5x5cm each arm),
680 two of which were surrounded by walls (enclosed arms). The apparatus was elevated 40 cm
681 above the ground. Each mouse was placed in the central square (neutral area) facing an open
682 arm, and time spent in the open and enclosed arms was measured for 5 min.

683 ***Open-field and Novel Object Location Test***

684 Hippocampal-dependent spatial and recognition memory was tested using the Novel Object
685 Location (NOL) test. The apparatus consisted of a square arena (45x45 cm), with cues in one
686 of the walls. Mice were allowed to freely explore for 30 min to habituate them to the arena.
687 Distance traveled and time spent in the center and the periphery were measured. On the
688 second day, two identical objects were placed equidistantly from walls, and mice were allowed
689 to explore for 10 min (NOL Acquisition). Twenty-four hours later, one of the objects was moved
690 to a novel position, and mice were allowed to explore for 5 min (NOL Testing). Object
691 preference was measured as the percentage of time exploring the novel object location.

692 ***Morris Water Maze***

693 Hippocampal-dependent spatial learning and memory were assessed using the Morris Water
694 Maze (MWM) task as previously described (Marzo et al., 2016). In the first phase, mice
695 performed four trials with a visible platform to check for deficiencies in vision or locomotion.
696 The escape platform was made visible by using a high-contrast top surface and attaching a

697 striped flag. In the second phase, mice were trained to find a hidden platform with extra-maze
698 visible cues for 6 days with 4 trials per day. The platform was submerged 2 cm below water
699 and placed at the midpoint of one of the quadrants. Each mouse was allowed to search for
700 the platform for up to 60 sec, after which mice that failed to reach the platform were placed on
701 the platform. All mice were left on the platform for 10 sec before they were returned to their
702 home cage. Probe trials were conducted before the fifth day of training (early probe) and 24h
703 after the last day of training (late probe). During the probe trials, the platform was removed
704 from the pool, and mice were allowed to swim for 60 sec.

705 **Human RNAseq analyses**

706 The reprocessed ROSMAP (De Jager et al., 2018), MSBB (Wang et al., 2018) and
707 MayoRNAseq (Allen et al., 2016) temporal cortex RNASeq datasets and their associated
708 phenotypic data such as Braak (Braak et al., 2006) and CERAD (Mirra et al., 1991) scores
709 were downloaded from the AMP-AD consortium
710 (https://www.synapse.org/#!Synapse:syn2580853/wiki/409840). For the ROSMAP study, AD
711 cases were defined as individuals with a cognitive diagnosis of AD with no other cause of
712 cognitive impairment (cogdx = 4 and cogdx = 5), and controls were defined as those with no
713 cognitive impairment (cogdx = 1). For the MSBB dataset, controls were defined as those with
714 a CERAD score of 1 (normal) and a clinical dementia rating (CDR) of 0 or 0.5 (no cognitive
715 deficits or questionable dementia respectively), whereas cases were defined as subjects with
716 CERAD score of 2, 3 or 4 (possible, probable, definite AD) and a CDR of 2 or greater (mild
717 dementia, moderate dementia, or severe to terminal dementia). For the MayoRNASeq
718 dataset, individuals were already classified as an AD case or control based on
719 neuropathology. All cases had a Braak stage of IV or greater. Controls had a Braak stage of
720 III or lower.

721 RNASeq datasets from ROSMAP (De Jager et al., 2018), MSBB (Wang et al., 2018), and
722 MayoRNAseq (Allen et al., 2016) underwent quality control using RNASeQC (DeLuca et al.,
723 2012) and were normalized for gene length and GC content with low expressed genes filtered
724 out. Following quality control and normalization, 16,485 genes remained in the analysis. Linear
725 mixed effect models (LMEM) in combination with principal component (PC) analyses were
726 performed on normalized counts to combine data and adjust for batch effects and hidden
727 confounders. LMEM used sex, age at death, and the first three principal components as fixed
728 effects, whilst individual ID and sequencing batch were used as random effects. Logistic
729 regression was then performed on residuals from the LMEM for AD case/control status (n =
730 379 AD cases, 248 controls). Ordinal regressions were also performed on residuals from the

731 LMEM for Braak stage (0-6) (n = 627) and CERAD scores (1-4) (n = 537). The β-coefficient
732 indicates the degree of differential *DKK3* expression.

733 **Statistical analyses**

734 All graphed data are displayed as mean ± SEM. Statistical analyses were performed using
735 GraphPad Prism version 8.0.2. Statistical outliers were determined using Grubbs and ROUT
736 tests. Dataset normality was tested by the D'Agostino and Pearson or Shapiro-Wilk tests.
737 When datasets passed normality, comparisons between two groups were analyzed using the
738 unpaired two-sided Student's T-test whilst comparisons between more than two groups used
739 one- or two- way ANOVA, followed by Tukey's multiple comparisons tests. For non-normally
740 distributed data, comparisons between two groups were performed using the Mann-Whitney
741 U test, and comparisons between more than two groups with Kruskal-Wallis followed by
742 Dunn's multiple comparison test. Pearson correlation coefficient was used for colocalization
743 analyses. In all graphs, N-numbers corresponding to the number of independent primary
744 cultures, animals, or human subjects, unless otherwise specified, are shown. In all figures, p-
745 values are depicted as: **p*-value≤0.05, ***p*-value≤0.01, ****p*-value≤0.001.

746 **ACKNOWLEDGMENTS**

747 We would like to thank Professors Takashi Saito and Takaomi Saido for the $APP^{NL-G-F}$ mice
748 and Professors Qingbo Xu for providing us with brain samples of the *DKK3*$^{-/-}$ *ApoE*$^{-/-}$ mice used
749 as controls for antibody validation. We thank members of the Salinas lab and our collaborators
750 Professors Francesca Cacucci and Alasdair Gibb for their support and discussion on this
751 project. We also thank Dr Ernest Palomer for his technical advice on qPCR analyses. The
752 results published here are in whole or in part based on data obtained from the AD Knowledge
753 Portal (https://adknowledgeportal.org). ROSMAP data were provided by the Rush Alzheimer's
754 Disease Center, Rush University Medical Center, Chicago. Data collection was supported
755 through funding by NIA grants P30AG10161 (ROS), R01AG15819 (ROSMAP; genomics and
756 RNAseq), R01AG17917 (MAP), R01AG30146, R01AG36042 (5hC methylation, ATACseq),
757 RC2AG036547 (H3K9Ac), R01AG36836 (RNAseq), R01AG48015 (monocyte RNAseq)
758 RF1AG57473 (single nucleus RNAseq), U01AG32984 (genomic and whole exome
759 sequencing), U01AG46152 (ROSMAP AMP-AD, targeted proteomics), U01AG46161(TMT
760 proteomics), U01AG61356 (whole genome sequencing, targeted proteomics, ROSMAP AMP-
761 AD), the Illinois Department of Public Health (ROSMAP), and the Translational Genomics
762 Research Institute (genomic). Additional phenotypic data can be requested at
763 www.radc.rush.edu. MSBB data were generated from postmortem brain tissue collected
764 through the Mount Sinai VA Medical Center Brain Bank and were provided by Dr. Eric Schadt

765 from Mount Sinai School of Medicine. The Mayo RNAseq study data was led by Dr. Nilüfer
766 Ertekin-Taner, Mayo Clinic, Jacksonville, FL as part of the multi-PI U01 AG046139 (MPIs
767 Golde, Ertekin-Taner, Younkin, Price). Samples were provided from the following sources:
768 The Mayo Clinic Brain Bank. Data collection was supported through funding by NIA grants
769 P50 AG016574, R01 AG032990, U01 AG046139, R01 AG018023, U01 AG006576, U01
770 AG006786, R01 AG025711, R01 AG017216, R01 AG003949, NINDS grant R01 NS080820,
771 CurePSP Foundation, and support from Mayo Foundation. Study data includes samples
772 collected through the Sun Health Research Institute Brain and Body Donation Program of Sun
773 City, Arizona. The Brain and Body Donation Program is supported by the National Institute of
774 Neurological Disorders and Stroke (U24 NS072026 National Brain and Tissue Resource for
775 Parkinsons Disease and Related Disorders), the National Institute on Aging (P30 AG19610
776 Arizona Alzheimers Disease Core Center), the Arizona Department of Health Services
777 (contract 211002, Arizona Alzheimers Research Center), the Arizona Biomedical Research
778 Commission (contracts 4001, 0011, 05-901 and 1001 to the Arizona Parkinson's Disease
779 Consortium) and the Michael J. Fox Foundation for Parkinsons Research. Diagrams included
780 in the figures were created with Biorender.com. This work was funded by Alzheimer's Society
781 (AS-PG-17-006), MRC (MR/S012125/1 and MR/M024083/1), Alzheimer's Research UK
782 (ARUK-PG2018A-002).

783 **AUTHOR CONTRIBUTIONS**

784 N.M.-F., M.P. and P.C.S. contributed to the conception and design of the study and the
785 interpretation of the results. N.M.-F. and M.P. generated and analyzed the results. F.M.
786 conducted and analyzed patch-clamp recording experiments. I.W. performed plaque staining
787 in AD mouse brains and contributed to synapse analyses. K.C., D.I., G.L., and V.E.-P.
788 performed human RNAseq studies. N.M.-F., M.P. and P.C.S. prepared the figures and wrote
789 the manuscript. All authors reviewed and approved the final version of this manuscript.

790

791 **DECLARATION OF INTERESTS**

792 The authors declare no competing interests.

793 **DATA AND MATERIALS AVAILABILITY**

794 All data are available in the main text or the supplementary materials.

## REFERENCES


Abarzua F, Sakaguchi M, Takaishi M, Nasu Y, Kurose K, Ebara S, Miyazaki M, Namba M, Kumon H, Huh N. 2005. Adenovirus-mediated overexpression of REIC/Dkk-3 selectively induces apoptosis in human prostate cancer cells through activation of c-Jun-NH2-kinase. *Cancer Research* **65**:9617–9622. doi:10.1158/0008-5472.CAN-05-0829

Alarcón MA, Medina MA, Hu Q, Avila ME, Bustos BI, Pérez-Palma E, Peralta A, Salazar P, Ugarte GD, Reyes AE, Martin GM, Opazo C, Moon RT, De Ferrari GV. 2013. A novel functional low-density lipoprotein receptor-related protein 6 gene alternative splice variant is associated with Alzheimer's disease. *Neurobiology of Aging* **34**:1709.e9–18. doi:10.1016/j.neurobiolaging.2012.11.004

Allen M, Carrasquillo MM, Funk C, Heavner BD, Zou F, Younkin CS, Burgess JD, Chai H-S, Crook J, Eddy JA, Li H, Logsdon B, Peters MA, Dang KK, Wang X, Serie D, Wang C, Nguyen T, Lincoln S, Malphrus K, Bisceglio G, Li M, Golde TE, Mangravite LM, Asmann Y, Price ND, Petersen RC, Graff-Radford NR, Dickson DW, Younkin SG, Ertekin-Taner N. 2016. Human whole genome genotype and transcriptome data for Alzheimer's and other neurodegenerative diseases. *Scientific data* **3**:160089. doi:10.1038/sdata.2016.89

Barrantes I del B, Montero-Pedrazuela A, Guadaño-Ferraz A, Obregon M-J, Martinez de Mena R, Gailus-Durner V, Fuchs H, Franz TJ, Kalaydjiev S, Klempt M, Hölter S, Rathkolb B, Reinhard C, Morreale de Escobar G, Bernal J, Busch DH, Wurst W, Wolf E, Schulz H, Shtrom S, Greiner E, Hrabé de Angelis M, Westphal H, Niehrs C. 2006. Generation and characterization of dickkopf3 mutant mice. *Molecular and Cellular Biology* **26**:2317–2326. doi:10.1128/MCB.26.6.2317-2326.2006

Braak H, Alafuzoff I, Arzberger T, Kretzschmar H, Del Tredici K. 2006. Staging of Alzheimer disease-associated neurofibrillary pathology using paraffin sections and immunocytochemistry. *Acta Neuropathologica* **112**:389–404. doi:10.1007/s00401-006-0127-z

Brewer WJ, Xet-Mull AM, Yu A, Sweeney MI, Walton EM, Tobin DM. 2022. Macrophage NFATC2 mediates angiogenic signaling during mycobacterial infection. *Cell Reports* **41**:111817. doi:10.1016/j.celrep.2022.111817

Bruggink KA, Kuiperij HB, Gloerich J, Otte-Höller I, Rozemuller AJM, Claassen JAHR, Küsters B, Verbeek MM. 2015. Dickkopf-related protein 3 is a potential A\beta-associated protein in Alzheimer's Disease. *Journal of Neurochemistry* **134**:1152–1162. doi:10.1111/jnc.13216

Caneparo L, Huang Y-L, Staudt N, Tada M, Ahrendt R, Kazanskaya O, Niehrs C, Houart C. 2007. Dickkopf-1 regulates gastrulation movements by coordinated modulation of Wnt/beta catenin and Wnt/PCP activities, through interaction with the Dally-like homolog Knypek. *Genes & Development* **21**:465–480. doi:10.1101/gad.406007

Caricasole A, Copani A, Caraci F, Aronica E, Rozemuller AJ, Caruso A, Storto M, Gaviraghi G, Terstappen GC, Nicoletti F. 2004. Induction of Dickkopf-1, a negative modulator of the Wnt pathway, is associated with neuronal degeneration in Alzheimer's brain. *The Journal of Neuroscience* **24**:6021–6027. doi:10.1523/JNEUROSCI.1381-04.2004

Caricasole A, Ferraro T, Iacovelli L, Barletta E, Caruso A, Melchiorri D, Terstappen GC, Nicoletti F. 2003. Functional characterization of WNT7A signaling in PC12 cells: interaction with A FZD5 x LRP6 receptor complex and modulation by Dickkopf proteins. *The Journal of Biological Chemistry* **278**:37024–37031. doi:10.1074/jbc.M300191200

Ciani L, Boyle KA, Dickins E, Sahores M, Anane D, Lopes DM, Gibb AJ, Salinas PC. 2011. Wnt7a signaling promotes dendritic spine growth and synaptic strength through $Ca^{2+}$/Calmodulin-dependent protein kinase II. *Proceedings of the National Academy of Sciences of the United States of America* **108**:10732–10737. doi:10.1073/pnas.1018132108

Clements JD, Bekkers JM. 1997. Detection of spontaneous synaptic events with an optimally scaled template. *Biophysical Journal* **73**:220–229. doi:10.1016/S0006-3495(97)78062-7

De Ferrari GV, Papassotiropoulos A, Biechele T, Wavrant De-Vrieze F, Avila ME, Major MB, Myers A, Sáez K, Henríquez JP, Zhao A, Wollmer MA, Nitsch RM, Hock C, Morris CM, Hardy J, Moon RT. 2007. Common genetic variation within the low-density lipoprotein receptor-related protein 6 and late-onset Alzheimer's disease. *Proceedings of the National Academy of Sciences of the United States of America* **104**:9434–9439. doi:10.1073/pnas.0603523104

De Jager PL, Ma Y, McCabe C, Xu J, Vardarajan BN, Felsky D, Klein H-U, White CC, Peters MA, Lodgson B, Nejad P, Tang A, Mangravite LM, Yu L, Gaiteri C, Mostafavi S, Schneider JA, Bennett DA. 2018. A multi-omic atlas of the human frontal cortex for aging and Alzheimer's disease research. *Scientific data* **5**:180142. doi:10.1038/sdata.2018.142

DeLuca DS, Levin JZ, Sivachenko A, Fennell T, Nazaire M-D, Williams C, Reich M, Winckler W, Getz G. 2012. RNA-SeQC: RNA-seq metrics for quality control and process optimization. *Bioinformatics* **28**:1530–1532. doi:10.1093/bioinformatics/bts196

Deuker L, Doeller CF, Fell J, Axmacher N. 2014. Human neuroimaging studies on the hippocampal CA3 region - integrating evidence for pattern separation and completion. *Frontiers in Cellular Neuroscience* **8**:64. doi:10.3389/fncel.2014.00064

Drummond E, Nayak S, Faustin A, Pires G, Hickman RA, Askenazi M, Cohen M, Haldiman T, Kim C, Han X, Shao Y, Safar JG, Ueberheide B, Wisniewski T. 2017. Proteomic differences in amyloid plaques in rapidly progressive and sporadic Alzheimer's disease. *Acta Neuropathologica* **133**:933–954. doi:10.1007/s00401-017-1691-0

Galli S, Lopes DM, Ammari R, Kopra J, Millar SE, Gibb A, Salinas PC. 2014. Deficient Wnt signalling triggers striatal synaptic degeneration and impaired motor behaviour in adult mice. *Nature Communications* **5**:4992. doi:10.1038/ncomms5992

Galli S, Stancheva SH, Dufor T, Gibb AJ, Salinas PC. 2021. Striatal synapse degeneration and dysfunction are reversed by reactivation of wnt signaling. *Frontiers in synaptic neuroscience* **13**:670467. doi:10.3389/fnsyn.2021.670467

Gomez-Suaga P, Mórotz GM, Markovinovic A, Martín-Guerrero SM, Preza E, Arias N, Mayl K, Aabdien A, Gesheva V, Nishimura A, Annibali A, Lee Y, Mitchell JC, Wray S, Shaw C, Noble W, Miller CCJ. 2022. Disruption of ER-mitochondria tethering and signalling in C9orf72-associated amyotrophic lateral sclerosis and frontotemporal dementia. *Aging Cell* **21**:e13549. doi:10.1111/acel.13549

He Q, Duguid I, Clark B, Panzanelli P, Patel B, Thomas P, Fritschy J-M, Smart TG. 2015. Interneuron- and GABA(A) receptor-specific inhibitory synaptic plasticity in cerebellar Purkinje cells. *Nature Communications* **6**:7364. doi:10.1038/ncomms8364

Hesse R, Hurtado ML, Jackson RJ, Eaton SL, Herrmann AG, Colom-Cadena M, Tzioras M, King D, Rose J, Tulloch J, McKenzie C-A, Smith C, Henstridge CM, Lamont D, Wishart TM, Spires-Jones TL. 2019. Comparative profiling of the synaptic proteome from Alzheimer's disease patients with focus on the APOE genotype. *Acta neuropathologica communications* **7**:214. doi:10.1186/s40478-019-0847-7

Hong S, Beja-Glasser VF, Nfonoyim BM, Frouin A, Li S, Ramakrishnan S, Merry KM, Shi Q, Rosenthal A, Barres BA, Lemere CA, Selkoe DJ, Stevens B. 2016. Complement and microglia mediate early synapse loss in Alzheimer mouse models. *Science* **352**:712–716. doi:10.1126/science.aad8373

Hu N-W, Klyubin I, Anwyl R, Rowan MJ. 2009. GluN2B subunit-containing NMDA receptor antagonists prevent Abeta-mediated synaptic plasticity disruption in vivo. *Proceedings of the National Academy of Sciences of the United States of America* **106**:20504–20509. doi:10.1073/pnas.0908083106

Jack CR, Bennett DA, Blennow K, Carrillo MC, Dunn B, Haeberlein SB, Holtzman DM, Jagust W, Jessen F, Karlawish J, Liu E, Molinuevo JL, Montine T, Phelps C, Rankin KP, Rowe CC, Scheltens P, Siemers E, Snyder HM, Sperling R, Contributors, Elliott C, Masliah E, Ryan L, Silverberg N. 2018. NIA-AA Research Framework: Toward a biological

definition of Alzheimer's disease. *Alzheimer's & Dementia* **14**:535–562. doi:10.1016/j.jalz.2018.02.018

Johnson ECB, Carter EK, Dammer EB, Duong DM, Gerasimov ES, Liu Y, Liu J, Betarbet R, Ping L, Yin L, Serrano GE, Beach TG, Peng J, De Jager PL, Haroutunian V, Zhang B, Gaiteri C, Bennett DA, Gearing M, Wingo TS, Wingo AP, Lah JJ, Levey AI, Seyfried NT. 2022. Large-scale deep multi-layer analysis of Alzheimer's disease brain reveals strong proteomic disease-related changes not observed at the RNA level. *Nat Neurosci* **25**:213–225. doi:10.1038/s41593-021-00999-y

Jones ME, Büchler J, Dufor T, Palomer E, Teo S, Martin-Flores N, Boroviak K, Metzakopian E, Gibb A, Salinas PC. 2023. A genetic variant of the Wnt receptor LRP6 accelerates synapse degeneration during aging and in Alzheimer's disease. *Sci Adv* **9**:eabo7421. doi:10.1126/sciadv.abo7421

Kamal A, Ramakers GM, Urban IJ, De Graan PN, Gispen WH. 1999. Chemical LTD in the CA1 field of the hippocampus from young and mature rats. *The European Journal of Neuroscience* **11**:3512–3516. doi:10.1046/j.1460-9568.1999.00769.x

Katsinelos T, Zeitler M, Dimou E, Karakatsani A, Müller H-M, Nachman E, Steringer JP, Ruiz de Almodovar C, Nickel W, Jahn TR. 2018. Unconventional Secretion Mediates the Trans-cellular Spreading of Tau. *Cell Reports* **23**:2039–2055. doi:10.1016/j.celrep.2018.04.056

Killick R, Ribe EM, Al-Shawi R, Malik B, Hooper C, Fernandes C, Dobson R, Nolan PM, Lourdusamy A, Furney S, Lin K, Breen G, Wroe R, To AWM, Leroy K, Causevic M, Usardi A, Robinson M, Noble W, Williamson R, Lunnon K, Kellie S, Reynolds CH, Bazenet C, Hodges A, Brion J-P, Stephenson J, Simons JP, Lovestone S. 2014. Clusterin regulates \beta-amyloid toxicity via Dickkopf-1-driven induction of the wnt-PCP-JNK pathway. *Molecular Psychiatry* **19**:88–98. doi:10.1038/mp.2012.163

Koffie RM, Hashimoto T, Tai H-C, Kay KR, Serrano-Pozo A, Joyner D, Hou S, Kopeikina KJ, Frosch MP, Lee VM, Holtzman DM, Hyman BT, Spires-Jones TL. 2012. Apolipoprotein E4 effects in Alzheimer's disease are mediated by synaptotoxic oligomeric amyloid-\beta. *Brain: A Journal of Neurology* **135**:2155–2168. doi:10.1093/brain/aws127

Krupnik VE, Sharp JD, Jiang C, Robison K, Chickering TW, Amaravadi L, Brown DE, Guyot D, Mays G, Leiby K, Chang B, Duong T, Goodearl AD, Gearing DP, Sokol SY, McCarthy SA. 1999. Functional and structural diversity of the human Dickkopf gene family. *Gene* **238**:301–313. doi:10.1016/S0378-1119(99)00365-0

Leroy K, Yilmaz Z, Brion J-P. 2007. Increased level of active GSK-3beta in Alzheimer's disease and accumulation in argyrophilic grains and in neurones at different stages of neurofibrillary degeneration. *Neuropathol Appl Neurobiol* **33**:43–55. doi:10.1111/j.1365-2990.2006.00795.x

Li S, Jin M, Koeglsperger T, Shepardson NE, Shankar GM, Selkoe DJ. 2011. Soluble A\beta oligomers inhibit long-term potentiation through a mechanism involving excessive activation of extrasynaptic NR2B-containing NMDA receptors. *The Journal of Neuroscience* **31**:6627–6638. doi:10.1523/JNEUROSCI.0203-11.2011

Liu C-C, Tsai C-W, Deak F, Rogers J, Penuliar M, Sung YM, Maher JN, Fu Y, Li X, Xu H, Estus S, Hoe H-S, Fryer JD, Kanekiyo T, Bu G. 2014. Deficiency in LRP6-mediated Wnt signaling contributes to synaptic abnormalities and amyloid pathology in Alzheimer's disease. *Neuron* **84**:63–77. doi:10.1016/j.neuron.2014.08.048

Ly PTT, Cai F, Song W. 2011. Detection of neuritic plaques in Alzheimer's disease mouse model. *Journal of Visualized Experiments*. doi:10.3791/2831

Marzo A, Galli S, Lopes D, McLeod F, Podpolny M, Segovia-Roldan M, Ciani L, Purro S, Cacucci F, Gibb A, Salinas PC. 2016. Reversal of synapse degeneration by restoring wnt signaling in the adult hippocampus. *Current Biology* **26**:2551–2561. doi:10.1016/j.cub.2016.07.024

McLeod F, Bossio A, Marzo A, Ciani L, Sibilla S, Hannan S, Wilson GA, Palomer E, Smart TG, Gibb A, Salinas PC. 2018. Wnt Signaling Mediates LTP-Dependent Spine Plasticity and AMPAR Localization through Frizzled-7 Receptors. *Cell reports* **23**:1060–1071. doi:10.1016/j.celrep.2018.03.119

McLeod F, Marzo A, Podpolny M, Galli S, Salinas P. 2017. Evaluation of synapse density in hippocampal rodent brain slices. *Journal of Visualized Experiments*. doi:10.3791/56153

McLeod F, Salinas PC. 2018. Wnt proteins as modulators of synaptic plasticity. *Current Opinion in Neurobiology* **53**:90–95. doi:10.1016/j.conb.2018.06.003

Meilandt WJ, Cisse M, Ho K, Wu T, Esposito LA, Scearce-Levie K, Cheng IH, Yu G-Q, Mucke L. 2009. Neprilysin overexpression inhibits plaque formation but fails to reduce pathogenic Abeta oligomers and associated cognitive deficits in human amyloid precursor protein transgenic mice. *The Journal of Neuroscience* **29**:1977–1986. doi:10.1523/JNEUROSCI.2984-08.2009

Meister M, Papatriantafyllou M, Nordström V, Kumar V, Ludwig J, Lui KO, Boyd AS, Popovic ZV, Fleming TH, Moldenhauer G, Nawroth PP, Gröne H-J, Waldmann H, Oelert T, Arnold B. 2015. Dickkopf-3, a tissue-derived modulator of local T-cell responses. *Frontiers in Immunology* **6**:78. doi:10.3389/fimmu.2015.00078

Mirra SS, Heyman A, McKeel D, Sumi SM, Crain BJ, Brownlee LM, Vogel FS, Hughes JP, van Belle G, Berg L. 1991. The Consortium to Establish a Registry for Alzheimer's Disease (CERAD). Part II. Standardization of the neuropathologic assessment of Alzheimer's disease. *Neurology* **41**:479–486. doi:10.1212/wnl.41.4.479

Mizobuchi Y, Matsuzaki K, Kuwayama K, Kitazato K, Mure H, Kageji T, Nagahiro S. 2008. REIC/Dkk-3 induces cell death in human malignant glioma. *Neuro-oncology* **10**:244–253. doi:10.1215/15228517-2008-016

Mucke L, Masliah E, Yu GQ, Mallory M, Rockenstein EM, Tatsuno G, Hu K, Kholodenko D, Johnson-Wood K, McConlogue L. 2000a. High-level neuronal expression of abeta 1-42 in wild-type human amyloid protein precursor transgenic mice: synaptotoxicity without plaque formation. *The Journal of Neuroscience* **20**:4050–4058.

Mucke L, Selkoe DJ. 2012. Neurotoxicity of amyloid \beta-protein: synaptic and network dysfunction. *Cold Spring Harbor perspectives in medicine* **2**:a006338. doi:10.1101/cshperspect.a006338

Mucke L, Yu GQ, McConlogue L, Rockenstein EM, Abraham CR, Masliah E. 2000b. Astroglial expression of human alpha(1)-antichymotrypsin enhances alzheimer-like pathology in amyloid protein precursor transgenic mice. *The American Journal of Pathology* **157**:2003–2010. doi:10.1016/s0002-9440(10)64839-0

Niehrs C. 2012. The complex world of WNT receptor signalling. *Nature Reviews Molecular Cell Biology* **13**:767–779. doi:10.1038/nrm3470

Niehrs C. 2006. Function and biological roles of the Dickkopf family of Wnt modulators. *Oncogene* **25**:7469–7481. doi:10.1038/sj.onc.1210054

Nusse R, Clevers H. 2017. Wnt/\beta-Catenin Signaling, Disease, and Emerging Therapeutic Modalities. *Cell* **169**:985–999. doi:10.1016/j.cell.2017.05.016

Palomer E, Martín-Flores N, Jolly S, Pascual-Vargas P, Benvegnù S, Podpolny M, Teo S, Vaher K, Saito T, Saido TC, Whiting P, Salinas PC. 2022. Epigenetic repression of Wnt receptors in AD: a role for Sirtuin2-induced H4K16ac deacetylation of Frizzled1 and Frizzled7 promoters. *Molecular Psychiatry*. doi:10.1038/s41380-022-01492-z

Plantevin Krenitsky V, Nadolny L, Delgado M, Ayala L, Clareen SS, Hilgraf R, Albers R, Hegde S, D'Sidocky N, Sapienza J, Wright J, McCarrick M, Bahmanyar S, Chamberlain P, Delker SL, Muir J, Giegel D, Xu L, Celeridad M, Lachowitzer J, Bennett B, Moghaddam M, Khatsenko O, Katz J, Fan R, Bai A, Tang Y, Shirley MA, Benish B, Bodine T, Blease K, Raymon H, Cathers BE, Satoh Y. 2012. Discovery of CC-930, an orally active anti-fibrotic JNK inhibitor. *Bioorganic & Medicinal Chemistry Letters* **22**:1433–1438. doi:10.1016/j.bmcl.2011.12.027

Purro SA, Dickins EM, Salinas PC. 2012. The secreted Wnt antagonist Dickkopf-1 is required for amyloid \beta-mediated synaptic loss. *The Journal of Neuroscience* **32**:3492–3498. doi:10.1523/JNEUROSCI.4562-11.2012

Redlingshöfer L, McLeod F, Chen Y, Camus MD, Burden JJ, Palomer E, Briant K, Dannhauser PN, Salinas PC, Brodsky FM. 2020. Clathrin light chain diversity regulates membrane deformation in vitro and synaptic vesicle formation in vivo. *Proceedings of the National*

*Academy of Sciences of the United States of America* **117**:23527–23538. doi:10.1073/pnas.2003662117

Ring DB, Johnson KW, Henriksen EJ, Nuss JM, Goff D, Kinnick TR, Ma ST, Reeder JW, Samuels I, Slabiak T, Wagman AS, Hammond M-EW, Harrison SD. 2003. Selective glycogen synthase kinase 3 inhibitors potentiate insulin activation of glucose transport and utilization in vitro and in vivo. *Diabetes* **52**:588–595. doi:10.2337/diabetes.52.3.588

Rosi MC, Luccarini I, Grossi C, Fiorentini A, Spillantini MG, Prisco A, Scali C, Gianfriddo M, Caricasole A, Terstappen GC, Casamenti F. 2010. Increased Dickkopf-1 expression in transgenic mouse models of neurodegenerative disease. *Journal of Neurochemistry* **112**:1539–1551. doi:10.1111/j.1471-4159.2009.06566.x

Saito T, Matsuba Y, Mihira N, Takano J, Nilsson P, Itohara S, Iwata N, Saido TC. 2014. Single App knock-in mouse models of Alzheimer's disease. *Nature Neuroscience* **17**:661–663. doi:10.1038/nn.3697

Selkoe DJ, Hardy J. 2016. The amyloid hypothesis of Alzheimer's disease at 25 years. *EMBO Molecular Medicine* **8**:595–608. doi:10.15252/emmm.201606210

Sellers KJ, Elliott C, Jackson J, Ghosh A, Ribe E, Rojo AI, Jarosz-Griffiths HH, Watson IA, Xia W, Semenov M, Morin P, Hooper NM, Porter R, Preston J, Al-Shawi R, Baillie G, Lovestone S, Cuadrado A, Harte M, Simons P, Srivastava DP, Killick R. 2018. Amyloid \beta synaptotoxicity is Wnt-PCP dependent and blocked by fasudil. *Alzheimer's & Dementia* **14**:306–317. doi:10.1016/j.jalz.2017.09.008

Szabo L, Cummins N, Paganetti P, Odermatt A, Papassotiropoulos A, Karch C, Götz J, Eckert A, Grimm A. 2023. ER-mitochondria contacts and cholesterol metabolism are disrupted by disease-associated tau protein. *EMBO reports* **24**:e57499. doi:10.15252/embr.202357499

Thompson CL, Pathak SD, Jeromin A, Ng LL, MacPherson CR, Mortrud MT, Cusick A, Riley ZL, Sunkin SM, Bernard A, Puchalski RB, Gage FH, Jones AR, Bajic VB, Hawrylycz MJ, Lein ES. 2008. Genomic anatomy of the hippocampus. *Neuron* **60**:1010–1021. doi:10.1016/j.neuron.2008.12.008

Walsh DM, Klyubin I, Fadeeva JV, Cullen WK, Anwyl R, Wolfe MS, Rowan MJ, Selkoe DJ. 2002. Naturally secreted oligomers of amyloid beta protein potently inhibit hippocampal long-term potentiation in vivo. *Nature* **416**:535–539. doi:10.1038/416535a

Wang M, Beckmann ND, Roussos P, Wang E, Zhou X, Wang Q, Ming C, Neff R, Ma W, Fullard JF, Hauberg ME, Bendl J, Peters MA, Logsdon B, Wang P, Mahajan M, Mangravite LM, Dammer EB, Duong DM, Lah JJ, Seyfried NT, Levey AI, Buxbaum JD, Ehrlich M, Gandy S, Katsel P, Haroutunian V, Schadt E, Zhang B. 2018. The Mount Sinai cohort of large-scale genomic, transcriptomic and proteomic data in Alzheimer's disease. *Scientific data* **5**:180185. doi:10.1038/sdata.2018.185

Xiong F, Ge W, Ma C. 2019. Quantitative proteomics reveals distinct composition of amyloid plaques in Alzheimer's disease. *Alzheimer's & Dementia* **15**:429–440. doi:10.1016/j.jalz.2018.10.006

Xu J, Patassini S, Rustogi N, Riba-Garcia I, Hale BD, Phillips AM, Waldvogel H, Haines R, Bradbury P, Stevens A, Faull RLM, Dowsey AW, Cooper GJS, Unwin RD. 2019. Regional protein expression in human Alzheimer's brain correlates with disease severity. *Communications Biology* **2**:43. doi:10.1038/s42003-018-0254-9

Ye C, Walsh DM, Selkoe DJ, Hartley DM. 2004. Amyloid beta-protein induced electrophysiological changes are dependent on aggregation state: N-methyl-D-aspartate (NMDA) versus non-NMDA receptor/channel activation. *Neuroscience Letters* **366**:320–325. doi:10.1016/j.neulet.2004.05.060

Yu B, Kiechl S, Qi D, Wang X, Song Y, Weger S, Mayr A, Le Bras A, Karamariti E, Zhang Z, Barco Barrantes ID, Niehrs C, Schett G, Hu Y, Wang W, Willeit J, Qu A, Xu Q. 2017. A Cytokine-Like Protein Dickkopf-Related Protein 3 Is Atheroprotective. *Circulation* **136**:1022–1036. doi:10.1161/CIRCULATIONAHA.117.027690

1066 Zhang Li, Sun C, Jin Y, Gao K, Shi X, Qiu W, Ma C, Zhang Lianfeng. 2017. Dickkopf 3 (Dkk3)
1067 Improves Amyloid-\beta Pathology, Cognitive Dysfunction, and Cerebral Glucose
1068 Metabolism in a Transgenic Mouse Model of Alzheimer's Disease. *Journal of*
1069 *Alzheimer's Disease* **60**:733–746. doi:10.3233/JAD-161254
1070 Zhang Y, Chen K, Sloan SA, Bennett ML, Scholze AR, O'Keeffe S, Phatnani HP, Guarnieri P,
1071 Caneda C, Ruderisch N, Deng S, Liddelow SA, Zhang C, Daneman R, Maniatis T,
1072 Barres BA, Wu JQ. 2014. An RNA-sequencing transcriptome and splicing database of
1073 glia, neurons, and vascular cells of the cerebral cortex. *The Journal of Neuroscience*
1074 **34**:11929–11947. doi:10.1523/JNEUROSCI.1860-14.2014
1075 Zhu Y, Demidov ON, Goh AM, Virshup DM, Lane DP, Bulavin DV. 2014. Phosphatase WIP1
1076 regulates adult neurogenesis and WNT signaling during aging. *The Journal of Clinical*
1077 *Investigation* **124**:3263–3273. doi:10.1172/JCI73015
1078

1079

1080 **MAIN FIGURES**

1081

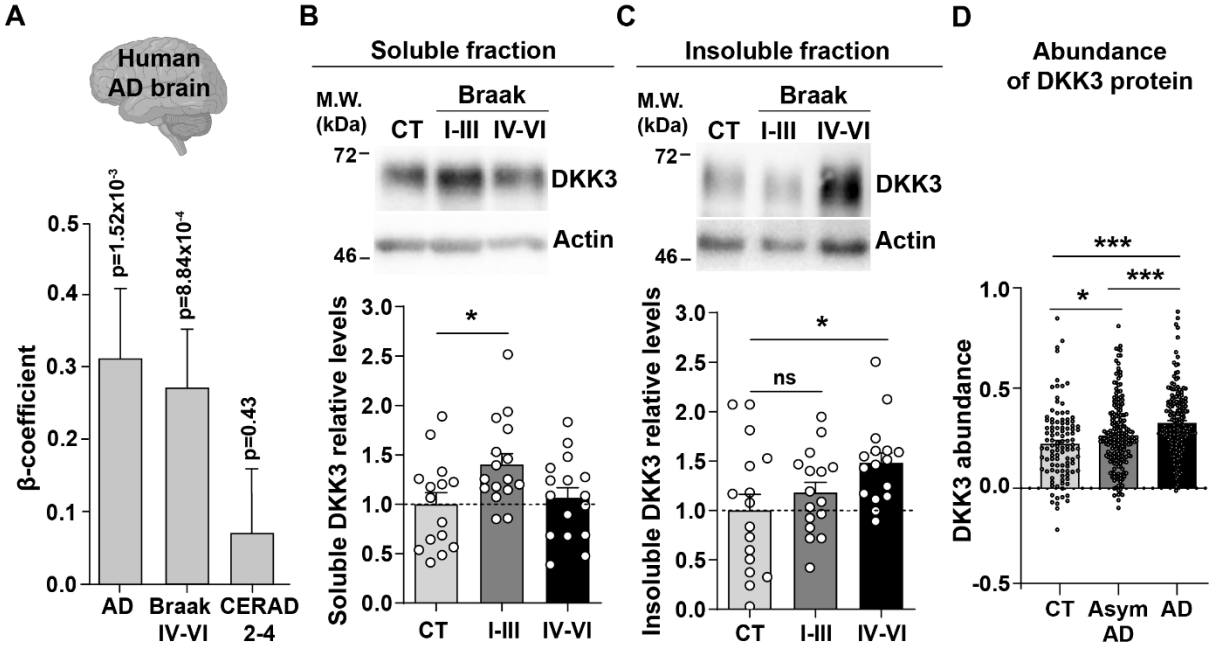


1082 **Figure 1**

1083 **Figure 1. DKK3 mRNA and protein levels are increased in the human AD brain.**

1084 (**A**) Temporal cortex RNAseq dataset logistic regression shows that *DKK3* mRNA levels are
1085 increased in AD cases relative to controls. Ordinal regression shows that *DKK3* is differentially
1086 expressed for Braak scores IV-VI but not for CERAD scores 2-4.

1087 (**B, C**) Representative immunoblots of DKK3 and loading control actin in (**B**) soluble and (**C**)
1088 insoluble protein fractions from the hippocampus of control (CT; n = 15-16), Braak stages I-III
1089 (n = 16), and Braak stage IV-VI (n = 16) individuals (One-Way ANOVA test followed by Tukey's
1090 multiple comparisons). See also **Table S1**.

1091 (**D**) Abundance of DKK3 protein in dorsolateral prefrontal cortex from control (CT, n = 106,
1092 asymptomatic (Asym) AD (n = 200), and AD (n = 182) individuals was evaluated using a
1093 tandem mass tag mass spectrometry (TMT-MS) proteomic dataset study (Johnson et al.,
1094 2022) (ANOVA with two-sided Holm correction, AD vs CT *p*-value = 0.00000168, Asym AD
1095 vs. CT *p*-value = 0.042492481, AD vs. Asym AD = 0.000402907).

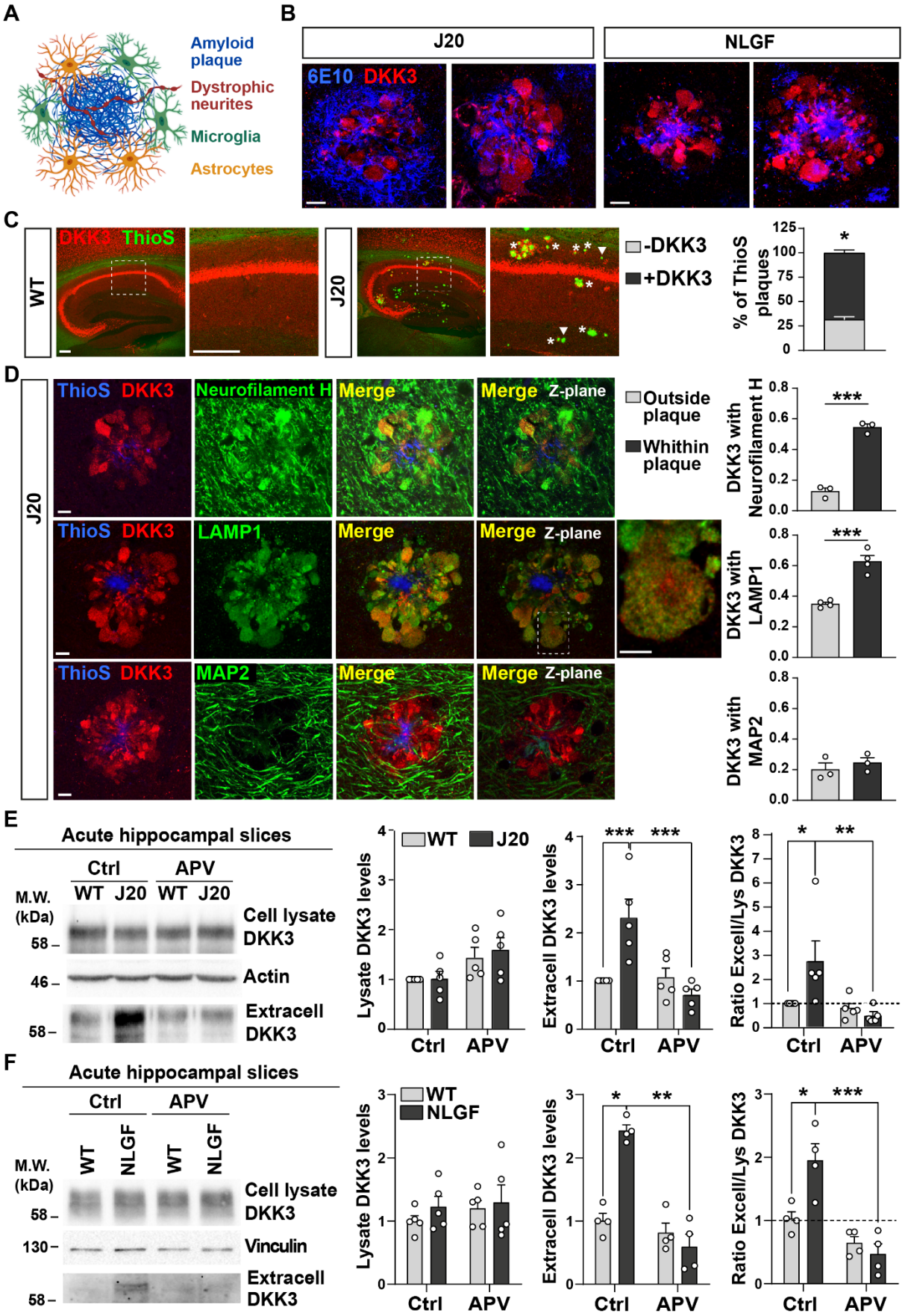


Figure 2

1096

1097 **Figure 2. DKK3 localizes to dystrophic neurites around Aβ plaques, and DKK3**
1098 **extracellular levels are increased in the brain of AD mouse models.**

1099 (**A**) Diagram of the components of an Aβ plaque (blue), astrocytes (orange), microglia (green),
1100 and dystrophic neurites (red).

1101 (**B**) Confocal images of DKK3 protein (red) and amyloid plaques stained with the 6E10
1102 antibody (blue) in the hippocampus of 18-month-old J20 and 8-months NLGF mice. Scale bar
1103 = 10 µm.

1104 (**C**) Confocal images of DKK3 (red) and Aβ plaques labeled by Thioflavin S (ThioS; green) in
1105 the hippocampus of 18-month-old WT and J20 mice. ThioS+ plaques not containing DKK3 (-
1106 DKK3; arrowheads), ThioS+ plaques containing DKK3 (+ DKK3; asterisks). Scale bar = 150
1107 µm and 100 µm in zoom-in pictures. Graph depicts quantification of the percentage of ThioS+
1108 plaques containing or not DKK3 (Student's T-test, n = 3 animals per genotype).

1109 (**D**) Z-stack confocal images show that DKK3 (red) accumulates at Aβ plaques (ThioS; blue)
1110 and colocalizes with atrophic axons (Neurofilament-H; green and LAMP1; green) but not with
1111 dendrites (MAP2; green). XY views of one plane are shown in the last panel. For LAMP1, a
1112 zoom-in picture showing colocalization between DKK3 and LAMP1 puncta is shown. Scale
1113 bar = 6 µm. Graphs show Pearson's correlation coefficient between DKK3 and Neurofilament-
1114 H, LAMP1, or MAP2, n = 3-4 animals.

1115 (**E, F**) Immunoblot images show DKK3 levels in the cell lysate and secreted fraction of acute
1116 hippocampal slices of (**E**) 3-4-month-old WT and J20 mice or (**F**) 2-3-months old WT and
1117 NLGF mice. Slices were incubated with vehicle (Ctrl) or APV for 3 hours. Actin or Vinculin was
1118 used as a loading control in the homogenate. Graphs show densitometric quantifications of
1119 lysate and extracellular (extracell) DKK3 levels relative to control and the ratio of
1120 extracellular/lysate DKK3 levels (Two-Way ANOVA followed by Tukey's post-hoc test; n = 4-
1121 5 animals).

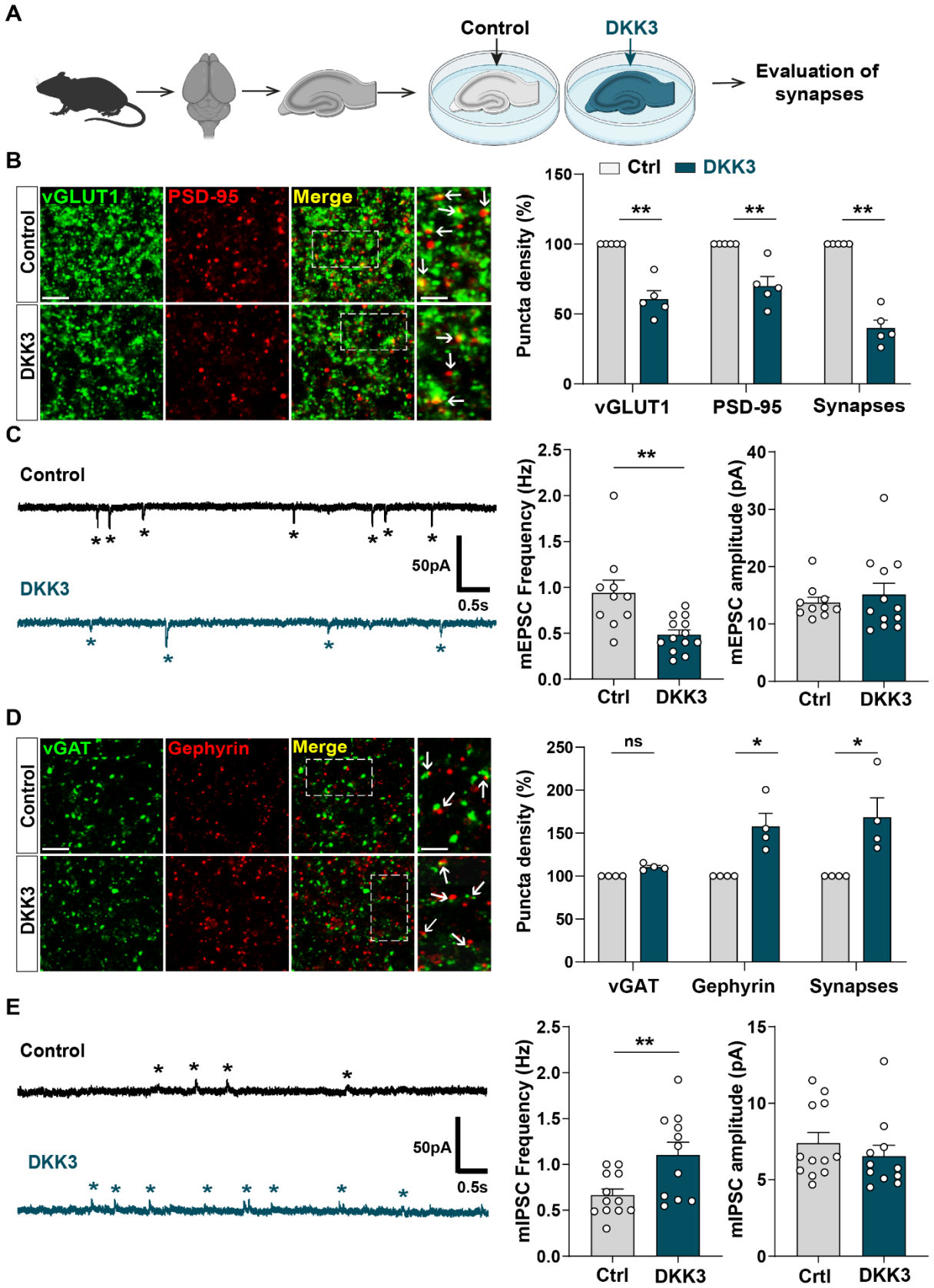
A
Control
DKK3
Evaluation of synapses
B
Control
DKK3
vGLUT1
PSD-95
Merge
Ctrl
DKK3
Puncta density (%)
vGLUT1
PSD-95
Synapses
C
Control
DKK3
50pA
0.5s
mEPSC Frequency (Hz)
mEPSC amplitude (pA)
Ctrl
DKK3
D
Control
DKK3
vGAT
Gephyrin
Merge
Puncta density (%)
ns
vGAT
Gephyrin
Synapses
E
Control
DKK3
50pA
0.5s
mIPSC Frequency (Hz)
mIPSC amplitude (pA)
Ctrl
DKK3

Figure 3

1124 **Figure 3. Gain-of-function of DKK3 leads to opposing effects on the number of**
1125 **excitatory and inhibitory synapses in the hippocampus.**

1126 (**A**) Diagram depicting the treatment of hippocampal brain slices obtained from 3-month-old
1127 adult WT mice with vehicle (Ctrl) or recombinant DKK3 protein. Synapses were evaluated by
1128 confocal microscopy and electrophysiological recordings.

1129 (**B**) Confocal images of the CA3 SR region labeled with the presynaptic excitatory marker
1130 vGLUT1 (green) and the postsynaptic marker PSD-95 (red). Arrows indicate excitatory
1131 synapses as colocalized pre- and postsynaptic puncta. Scale bar = 5 µm and 2.5 µm in
1132 zoomed-in pictures. Quantification is shown on the right-hand side (Mann-Whitney test, n = 5
1133 animals per condition).

1134 (**C**) Representative mEPSC traces recorded at -60mV from CA3 cells. Stars indicate mEPSC
1135 events. Quantification of mEPSC frequency and amplitude is shown on the right-hand side
1136 (Mann-Whitney test, n = 10-13 cells from 5 animals).

1137 (**D**) Confocal images of the CA3 SR region labeled with the presynaptic inhibitory marker vGAT
1138 (green) and the postsynaptic marker gephyrin (red). Arrows indicate inhibitory synapses as
1139 colocalized pre- and postsynaptic puncta. Scale bar = 5 µm and 2.5 µm in zoomed-in pictures.
1140 Quantification is shown on the right-hand side (Mann-Whitney test, n = 4 animals per
1141 condition).

1142 (**E**) Representative mIPSC traces recorded at 0mV from CA3 cells. Stars indicate mIPSC
1143 events. Quantification of mIPSC frequency and amplitude is shown on the right-hand side
1144 (Student's T-test for mIPSC frequency and Mann-Whitney test for mIPSC amplitude, n = 11-
1145 12 cells from 5-7 animals).

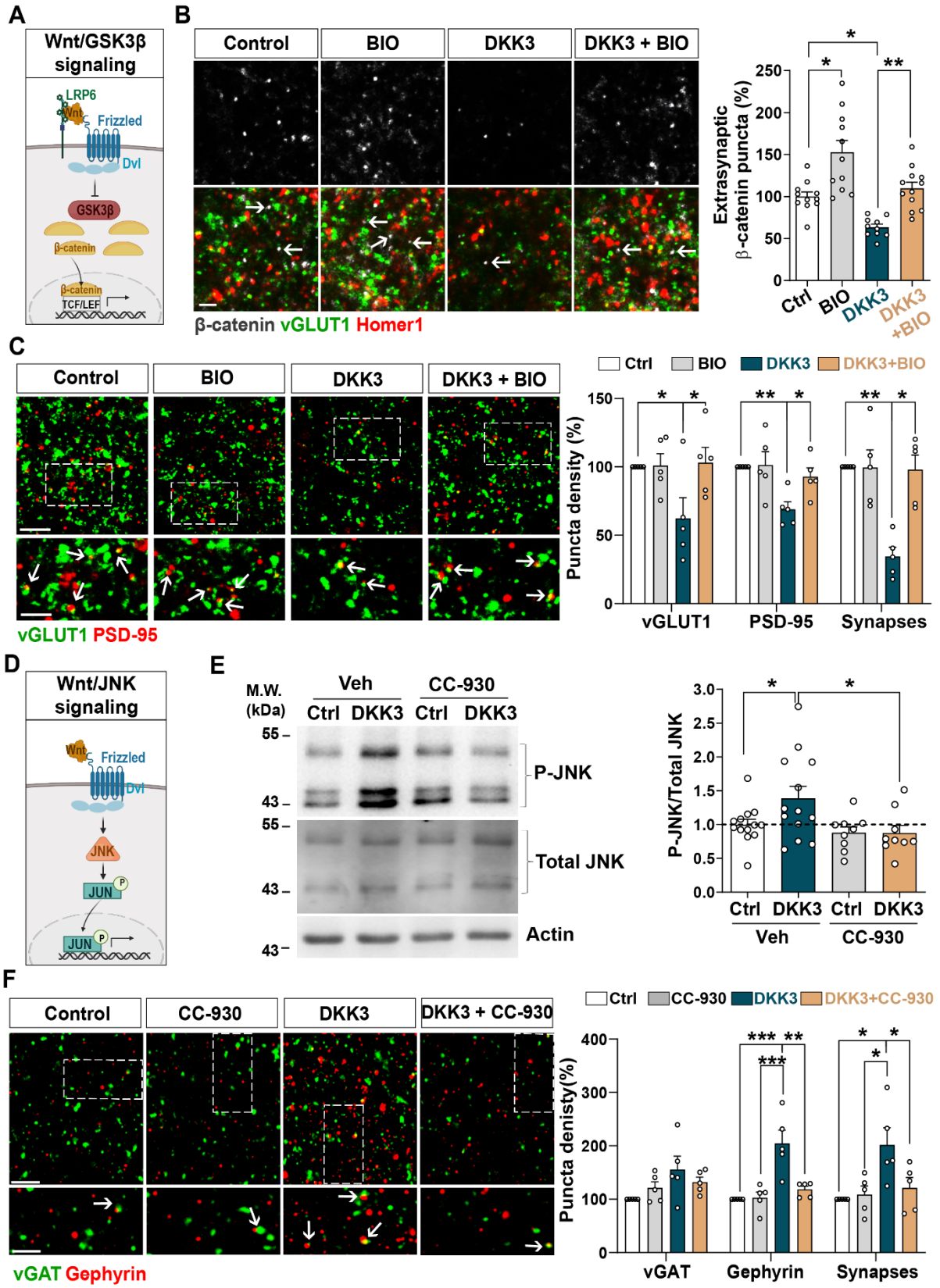
A
Wnt/GSK3β signaling
LRP6
Wnt
Frizzled
Dvl
GSK3β
β-catenin
β-catenin
TCF/LEF
B
Control
BIO
DKK3
DKK3 + BIO
β-catenin vGLUT1 Homer1
Extrasynaptic β-catenin puncta (%)
Ctrl
BIO
DKK3
DKK3 +BIO
C
Control
BIO
DKK3
DKK3 + BIO
vGLUT1 PSD-95
Ctrl
BIO
DKK3
DKK3+BIO
Puncta density (%)
vGLUT1
PSD-95
Synapses
D
Wnt/JNK signaling
Wnt
Frizzled
Dvl
JNK
JUN
JUN
E
M.W. (kDa)
Veh
CC-930
Ctrl
DKK3
Ctrl
DKK3
P-JNK
Total JNK
Actin
P-JNK/Total JNK
Ctrl
DKK3
Ctrl
DKK3
Veh
CC-930
F
Control
CC-930
DKK3
DKK3 + CC-930
vGAT Gephyrin
Ctrl
CC-930
DKK3
DKK3+CC-930
Puncta denisty(%)
vGAT
Gephyrin
Synapses

Figure 4

1148 **Figure 4. DKK3 regulates excitatory and inhibitory synapse number through the**
1149 **Wnt/GSK3β and Wnt/JNK pathways respectively.**

1150 (**A**) Diagram of the canonical Wnt pathway through inhibition of GSK3β (Wnt/GSK3β pathway),
1151 resulting in elevation of β-catenin and transcriptional activation via TCF/LEF.

1152 (**B**) Confocal images show excitatory synapses, visualized by colocalization of vGLUT1
1153 (green) and Homer1 (red), as well as β-catenin puncta (grey) in the CA3 SR after treatment
1154 with vehicle (Ctrl) or DKK3 in the absence or presence of BIO. Arrows indicate extra-synaptic
1155 β-catenin puncta. Scale bar = 5 μm. Quantification of extrasynaptic β-catenin puncta density
1156 as a percentage of control is shown on the right-hand side (Two-Way ANOVA followed by
1157 Tukey's multiple comparisons, n = 2-3 brain slices/animal from 5 animals).

1158 (**C**) Confocal images show excitatory synapses (co-localized vGLUT1 puncta in green and
1159 PSD-95 puncta in red) in the CA3 SR after treatment with vehicle (Ctrl) or DKK3 in the absence
1160 or presence of BIO. Scale bar = 5 μm and 2.5 μm. Graph shows the quantification of puncta
1161 density of pre- and postsynaptic markers and excitatory synapses as a percentage of control
1162 (Kruskal-Wallis followed by Dunn's multiple comparisons, n = 5 animals).

1163 (**D**) Diagram of the Wnt pathway through activation of JNK (Wnt/JNK pathway), resulting in
1164 increased levels of phospho-JNK and transcriptional changes.

1165 (**E**) Representative immunoblots of phospho-JNK Thr183/Tyr185 (P-JNK) and total JNK of
1166 brain slices treated with DKK3 and/or the JNK inhibitor CC-930. Actin was used as a loading
1167 control. Graph shows densitometric quantification of P-JNK vs. total JNK relative to the control
1168 condition (Kruskal-Wallis followed by Dunn's multiple comparisons, n = 2 brain slices/animal
1169 from 4-5 animals).

1170 (**F**) Confocal images showing inhibitory synapses defined by the colocalization of vGAT
1171 (green) and gephyrin (red) puncta in the CA3 SR after treatment with vehicle (Ctrl) or DKK3
1172 in the absence or presence of CC-930. Scale bar = 5 μm and 2.5 μm. Graph shows the
1173 quantification of puncta density of pre and postsynaptic markers and inhibitory synapses as a
1174 percentage of control (Kruskal-Wallis followed by Dunn's multiple comparisons, n = 5 animals).

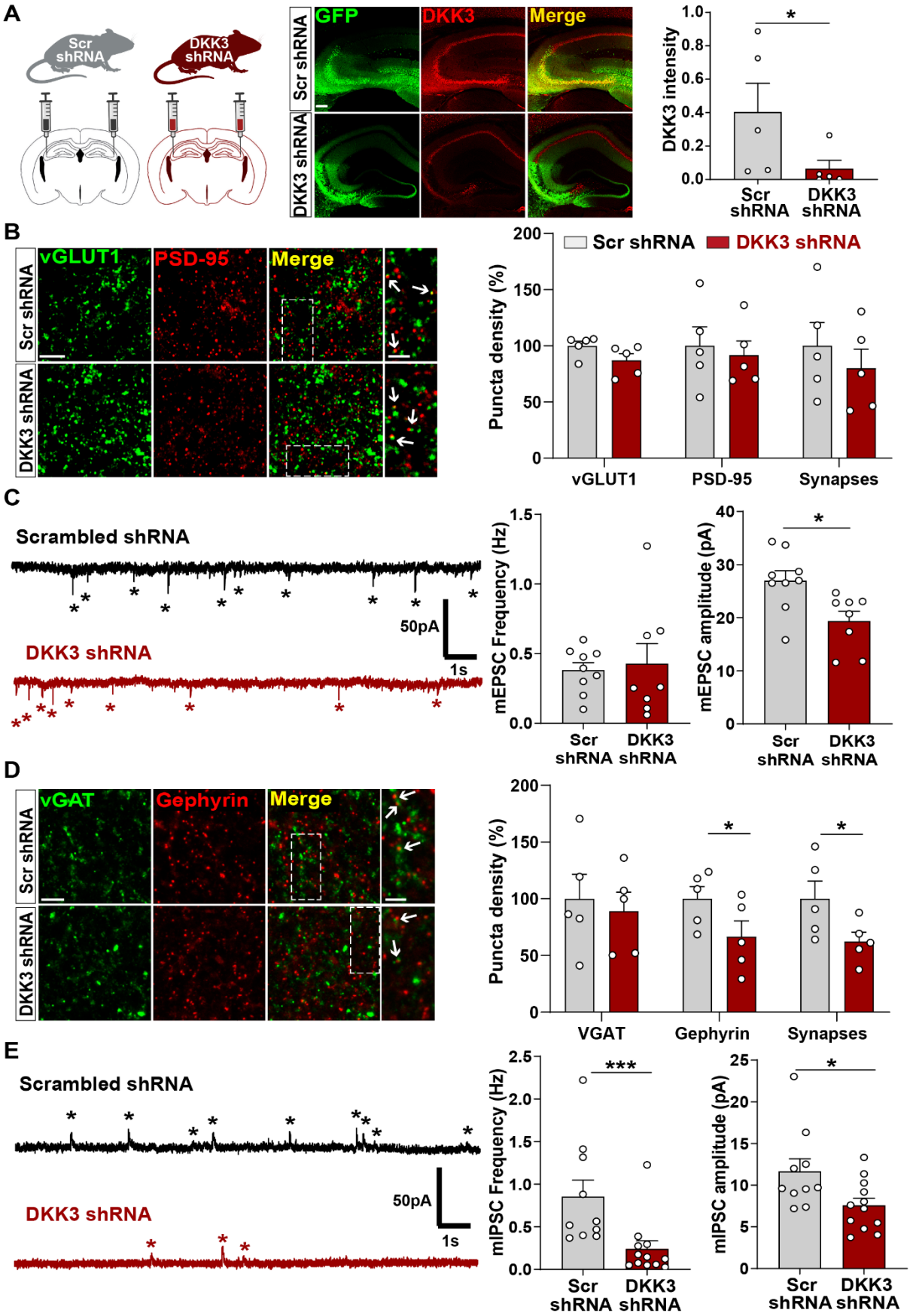
A
Scr shRNA
DKK3 shRNA
GFP
DKK3
Merge
DKK3 intensity
Scr shRNA
DKK3 shRNA
B
vGLUT1
PSD-95
Merge
Puncta density (%)
vGLUT1
PSD-95
Synapses
C
Scrambled shRNA
DKK3 shRNA
50pA
1s
mEPSC Frequency (Hz)
mEPSC amplitude (pA)
D
vGAT
Gephyrin
Merge
VGAT
Gephyrin
Synapses
E
Scrambled shRNA
DKK3 shRNA
50pA
1s
mIPSC Frequency (Hz)
mIPSC amplitude (pA)

Figure 5

1176 **Figure 5. *In vivo* loss-of-function of DKK3 decreases inhibitory synapses but does not**
1177 **affect excitatory synapses in the wild-type hippocampus.**

1178 (**A**) Diagram showing the experimental design. 3-month-old WT mice were injected with AAV9
1179 scrambled (Scr) or DKK3 shRNA in the CA3 region. Confocal images showing GFP (green)
1180 and DKK3 (red) in Scr- and DKK3-shRNA injected hippocampus. Scale bar = 145 µm. Graph
1181 shows quantification of DKK3 intensity in the area injected with the viruses.

1182 (**B**) Confocal images from CA3 SR show excitatory synapses (colocalized vGLUT1 puncta in
1183 green and PSD-95 puncta in red). Arrows indicate excitatory synapses. Scale bar = 5 µm and
1184 2.5 µm in zoomed-in images. Quantification is shown on the right-hand side (Student's T-test,
1185 n = 5 animals per condition).

1186 (**C**) Representative mEPSC traces recorded at -60mV from CA3 cells. Stars indicate mEPSC
1187 events. Quantification of mEPSC frequency and amplitude is shown on the right-hand side
1188 (Student's T-test, n = 8-9 cells from 4 animals).

1189 (**D**) Confocal images from CA3 SR show inhibitory synapses (colocalized vGAT in green and
1190 gephyrin in red). Arrows point to inhibitory synapses. Scale bar = 5 µm and 2.5 µm in zoomed-
1191 in pictures. Quantification is shown on the right-hand side (Student's T-test, n = 5 animals).

1192 (**E**) Representative mIPSC traces recorded at 0mV from CA3 cells. Stars indicate mIPSC
1193 events. Quantification of mIPSC frequency and amplitude is shown on the right-hand side
1194 (Mann-Whitney test, n = 10-12 cells from 6 animals).

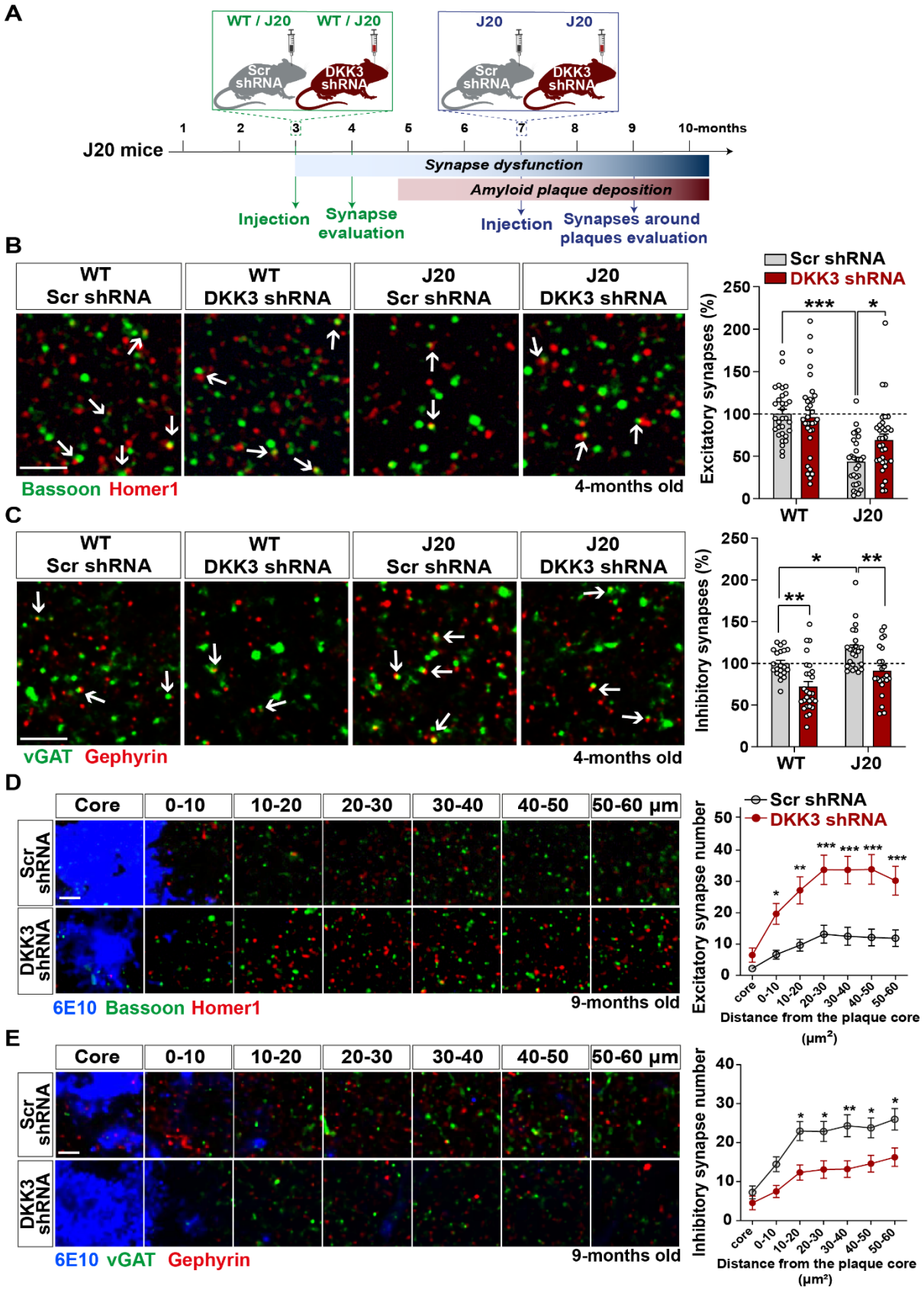
A
WT / J20
WT / J20
Scr shRNA
DKK3 shRNA
J20
J20
Scr shRNA
DKK3 shRNA
J20 mice
1
2
3
4
5
6
7
8
9
10-months
Synapse dysfunction
Amyloid plaque deposition
Injection
Synapse evaluation
Injection
Synapses around plaques evaluation
B
WT Scr shRNA
WT DKK3 shRNA
J20 Scr shRNA
J20 DKK3 shRNA
Bassoon Homer1
4-months old
Scr shRNA
DKK3 shRNA
Excitatory synapses (%)
WT
J20
C
WT Scr shRNA
WT DKK3 shRNA
J20 Scr shRNA
J20 DKK3 shRNA
vGAT Gephyrin
4-months old
Inhibitory synapses (%)
WT
J20
D
Core
0-10
10-20
20-30
30-40
40-50
50-60 µm
Scr shRNA
DKK3 shRNA
6E10 Bassoon Homer1
9-months old
Scr shRNA
DKK3 shRNA
Excitatory synapse number
core
0-10
10-20
20-30
30-40
40-50
50-60
Distance from the plaque core (µm²)
E
Core
0-10
10-20
20-30
30-40
40-50
50-60 µm
Scr shRNA
DKK3 shRNA
6E10 vGAT Gephyrin
9-months old
Inhibitory synapse number
core
0-10
10-20
20-30
30-40
40-50
50-60
Distance from the plaque core (µm²)

**Figure 6**

1197 **Figure 6. *In vivo* loss-of-function of DKK3 ameliorates synaptic changes in the**
1198 **hippocampus of J20 mice before and after Aβ plaque formation.**

1199 (**A**) Diagram depicting the experimental design. In green, 3-month-old WT and J20 mice were
1200 injected bilaterally with AAV9-Scr shRNA or AAV9-DKK3 shRNA in the CA3 region. The
1201 density of synapses was evaluated at 4-month-old before plaque deposition starts. In blue, 7-
1202 month-old J20 mice were injected bilaterally with AAV9-Scr shRNA or AAV9-DKK3 shRNA in
1203 the CA3 region. The density of synapses around plaques was evaluated at 9-month-old.

1204 (**B, C**) Representative confocal images from the CA3 SR region of 4-month-old WT and J20
1205 mice. Images show (**B**) excitatory synapses (Bassoon in green and Homer1 in red) and (**C**)
1206 inhibitory synapses (vGAT in green and Gephyrin in red). Arrows point to synapses. Scale bar
1207 = 2.5 μm. Quantification of synapse number as a percentage relative to WT-Scr shRNA
1208 animals is shown on the right-hand side (Two-Way ANOVA followed by Tukey's post-hoc test,
1209 n = 9-11 animals per condition and 2-3 brain slices per animal).

1210 (**D, E**) Representative confocal images from the CA3 SR region of 9-month-old J20 mice.
1211 Images show an Aβ plaque (6E10; blue) and (**D**) excitatory synapses or (**C**) inhibitory
1212 synapses at different distances relative to the core of the plaque. Scale bar = 2.5 μm. Graphs
1213 show synapse number per 200 $\mu m^3$ at each distance (Two-Way ANOVA followed by Tukey's
1214 post-hoc test, n = 6-7 animals per condition and 2-3 brain slices per animal).

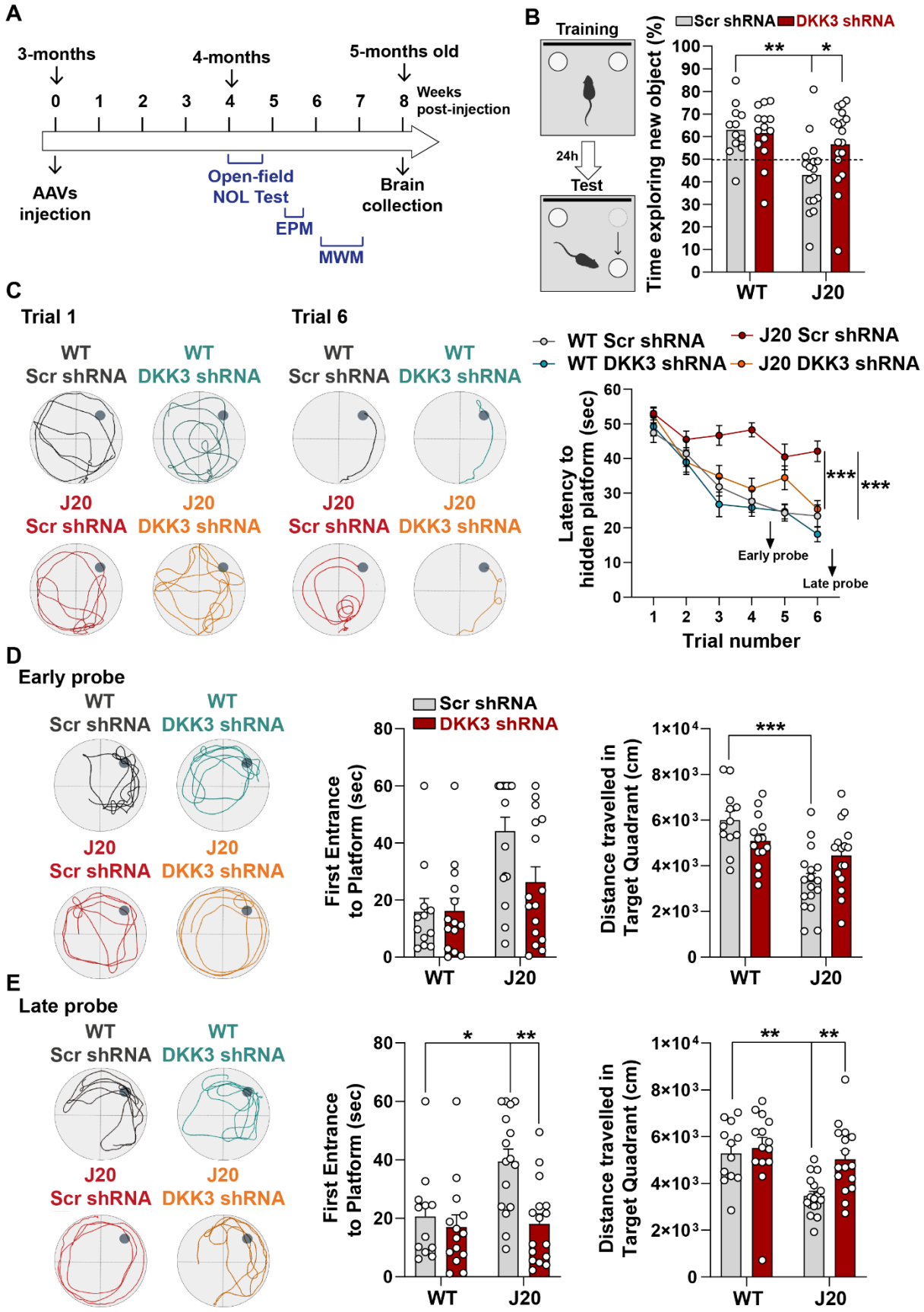
A
3-months
4-months
5-months old
0 1 2 3 4 5 6 7 8
Weeks post-injection
AAVs injection
Open-field
NOL Test
EPM
MWM
Brain collection
B
Training
24h
Test
Scr shRNA
DKK3 shRNA
Time exploring new object (%)
WT
J20
C
Trial 1
Trial 6
WT Scr shRNA
WT DKK3 shRNA
J20 Scr shRNA
J20 DKK3 shRNA
Latency to hidden platform (sec)
Early probe
Late probe
Trial number
D
Early probe
First Entrance to Platform (sec)
Distance travelled in Target Quadrant (cm)
E
Late probe

Figure 7

1217 **Figure 7. *In vivo* loss-of-function of DKK3 improves spatial memory in J20 mice.**

1218 (**A**) Diagram depicting that 3-month-old WT and J20 mice were injected bilaterally with AAV9-
1219 Scr shRNA or AAV9-DKK3 shRNA in the CA3 area of the hippocampus. One month later, the
1220 behavior of animals was assessed using the Open-field, Novel Object Location (NOL) test,
1221 Elevated-Plus Maze (EPM), and the Morris water maze (MWM).

1222 (**B**) Novel Object Location Test. The percentage of time exploring the new object location
1223 *versus* the total time was evaluated (Two-Way ANOVA with Tukey's post-hoc test, n = 12 WT
1224 Scr shRNA, 14 WT DKK3 shRNA, 17 J20 Scr shRNA, 16 J20 DKK3 shRNA).

1225 (**C- E**) Morris Water Maze.

1226 (**C**) Representative traces for the MWM Trials 1 and 6 are shown. Graph on the right shows
1227 the escape latency. Two-way ANOVA with repeated measures showed a significant effect
1228 over trials (animal group $F_{(3,55)} = 16.97$, *p*-value<0.0001; trial $F_{(5,259)} = 42.94$, *p*-value = 0.457;
1229 animal group and trial interaction $F_{(15,275)} = 2.753$, *p*-value = 0.0006). For all analyses (n=12
1230 WT Scr shRNA, 14 WT DKK3 shRNA, 17 J20 Scr shRNA, 16 J20 DKK3 shRNA). Graph show
1231 comparison between groups (Two-way ANOVA followed by Tukey's multiple comparisons).

1232 (**D, E**) Representative traces for the (D) Early and (E) Late probes. Graphs on the right show
1233 the time (sec) to first reach the target location (Kruskal Wallis followed by Dunns' multiple
1234 comparisons) and the distance (cm) traveled in the target quadrant (Two-way ANOVA followed
1235 by Tukey's post-hoc test for the early trial or Kruskal Wallis followed by Dunns' multiple
1236 comparisons).

1237